Metadata of the chapter that will be visualized online

Chapter Title	Analysis of Photoelectrochemical Systems by Impedance Spectroscopy	
Copyright Year	2016	
Copyright Holder	Springer International Publishing Switzerland	

Corresponding Author	Family Name	**Bisquert**
	Particle	
	Given Name	**Juan**
	Suffix	
	Division	Institute of Advanced Materials (INAM)
	Organization	Universitat Jaume I
	Address	Castelló 12006, Spain
	Email	bisquert@uji.es
Author	Family Name	**Gimenez**
	Particle	
	Given Name	**Sixto**
	Suffix	
	Division	Institute of Advanced Materials (INAM)
	Organization	Universitat Jaume I
	Address	Castelló 12006, Spain
	Email	sjulia@uji.es
Author	Family Name	**Bertoluzzi**
	Particle	
	Given Name	**Luca**
	Suffix	
	Division	Institute of Advanced Materials (INAM)
	Organization	Universitat Jaume I
	Address	Castelló 12006, Spain
	Email	bertoluz@uji.es
Author	Family Name	**Herraiz-Cardona**
	Particle	
	Given Name	**Isaac**
	Suffix	
	Division	Institute of Advanced Materials (INAM)
	Organization	Universitat Jaume I
	Address	Castelló 12006, Spain
	Email	iherraiz@uji.es

Abstract	The operation of photovoltaic and photoelectrochemical systems based on semiconductors that absorb visible light involves a variety of electronic

processes in the semiconductor that are followed by charge extraction and photoelectrochemical reactions at the solid/liquid interface. In recent years, a wide variety of semiconductor systems have been developed, and an increasingly complex structure of the catalyzed surface, nanostructured morphologies, and tandem configurations are being investigated. Here we describe the application of frequency-modulated impedance spectroscopy to provide mechanistic information about the different kinetic steps, as well as the distribution of energetic features as band bending and flat band potentials. The paper is focused on the interpretation of impedance spectroscopy results that contain key information about the photoelectrochemical performances of semiconductor systems. In particular, we investigate the origin of cathodic shift in water oxidation reaction due to different surface treatments, and we distinguish the effects of variation of recombination and charge transfer kinetics based on the equivalent circuit that can be established from impedance spectroscopy measurements.

Chapter 6
Analysis of Photoelectrochemical Systems by Impedance Spectroscopy

Juan Bisquert, Sixto Gimenez, Luca Bertoluzzi, and Isaac Herraiz-Cardona

6.1 Introduction

The development of efficient semiconductor structures for photoelectrochemical (PEC) fuel production from sunlight relies on the combination of fundamental semiconductor and catalytic properties as well as the coupling of different kinetic steps, to facilitate the forward flux of electronic/ionic processes, from charge generation to the electrochemical reaction at interfaces, that finally must be coupled in a cell structure that combines anodic and cathodic reactions. The aim of frequency-based characterization tools is to extract information about the internal kinetic and charge storage steps in the semiconductor electrodes and/or buried junctions, in order to discover the mechanistic operation of the system and to assess causes for efficiency or failure of it. Frequency methods operate at a given value of steady state of the system and introduce the small perturbation of a variable like voltage or light intensity. The resulting output provides a transfer function or impedance that constitutes a spectroscopy with high resolution of kinetic processes in a wide window of frequencies. Methods such as Impedance Spectroscopy (IS) are part of the standard tool kit in fields like electrochemistry and have been long used in photoelectrochemistry (Tench and Gerischer 1977). Light-modulated techniques are less widespread but also provide important insights (Peter 1990). This chapter will focus on IS applied to the understanding of PEC operation in relation to the efficient operation of semiconductor electrodes.

The foundations of IS applied to dye-sensitized solar cells have been previously described and will be taken as a basis here (Bisquert and Fabregat-Santiago 2010). A very large number of theoretical and experimental results of IS have been reported in the literature, and we do not provide a comprehensive review but focus on a number of main results and methods. We will address recent applications

J. Bisquert (✉) • S. Gimenez • L. Bertoluzzi • I. Herraiz-Cardona
Institute of Advanced Materials (INAM), Universitat Jaume I, Castelló 12006, Spain
e-mail: bisquert@uji.es; sjulia@uji.es; bertoluz@uji.es; iherraiz@uji.es

30 of several important and well-established concepts, such as the crucial role of
31 surface states in electron or hole transfer to acceptors in solution, and the band
32 edge shift by charging of the Helmholtz layer (Freund and Morrison 1968; Kelly
33 and Memming 1982; Allongue and Cachet 1984; Li and Peter 1985;
34 Vanmaekelbergh 1997). The chapter will focus on the recent developments of IS
35 models and measurements for the analysis of the performance of the dominant types
36 of semiconductors for water splitting, especially the set of wide bandgap metal
37 oxides TiO_2, Fe_2O_3, $BiVO_4$, WO_3, and their surface modifications. The chapter is
38 devoted to the main question of the operation of photoelectrodes; therefore, a main
39 theme treated here is which knowledge can be gained from the frequency scan
40 about the steady-state operation in fuel production regime. We will also describe
41 some recent advances in the modeling and understanding of PEC operation
42 (Bertoluzzi et al. 2016). Fundamental properties of the semiconductor
43 photoelectrodes have been discussed in Chap. 1 by L. M. Peter. Further ideas
44 about the application of IS methods in PEC systems will be introduced in
45 Sect. 6.2. Then we will treat a number of models of a semiconductor electrode
46 that can be adapted to different situations. The different types of models that we use
47 in this chapter are summarized in Fig. 6.1. We further discuss the types of structures
48 that will be the main object of analysis in this chapter.

49   Figure 6.1a shows a simple semiconductor layer where light absorption gener-
50 ates electrons and holes. In this model, the internal operation of the semiconductor
51 layer is rather simple and one can focus on the properties of charge transfer at the
52 surface. The bands are flat, indicating a small thickness that does not allow band
53 bending. Charge transport to the interfaces occurs by diffusion and the electrode
54 requires charge selectivity at the interfaces for PEC operation to occur. At the left
55 side of Fig. 6.1a, the redox reaction of holes transfer is favored over the electron
56 injection by kinetic or energetic reasons. At the right side of Fig. 6.1a, the selective
57 contact must extract only electrons toward the complementary electrode in the cell.
58 This simple model is very useful for the development of basic impedance models
59 that illustrate the competition between recombination and charge extraction
60 (Bertoluzzi and Bisquert 2012).

61   Figure 6.1b shows a one-dimensional model that contains a depletion region
62 (band bending) at the semiconductor/electrolyte interface. This is the classical
63 model for a PEC semiconductor electrode and its whose operation is illustrated in
64 more details in Fig. 6.2a, through the energy diagram of an n-type semiconductor.
65 This model provides a more realistic approach of the carrier dynamics inside the
66 semiconductor layer, and such traffic of carriers can be coupled to the charge
67 transfer and surface recombination events using numerical simulation, as discussed
68 in Sect. 6.3. In Fig. 6.2a, the left contact equilibrates with redox potential of the
69 relevant redox electrolyte and forms a depletion layer that will assist charge
70 collection as indicated in Fig. 6.2b. The total charge collection length is the addition
71 of the depletion layer w and one diffusion length of the minority carrier, L_p. The
72 optical absorption coefficient α determines the light penetration length $L_\alpha = \alpha^{-1}$
73 that should be shorter than charge collection length for optimal photon utilization.
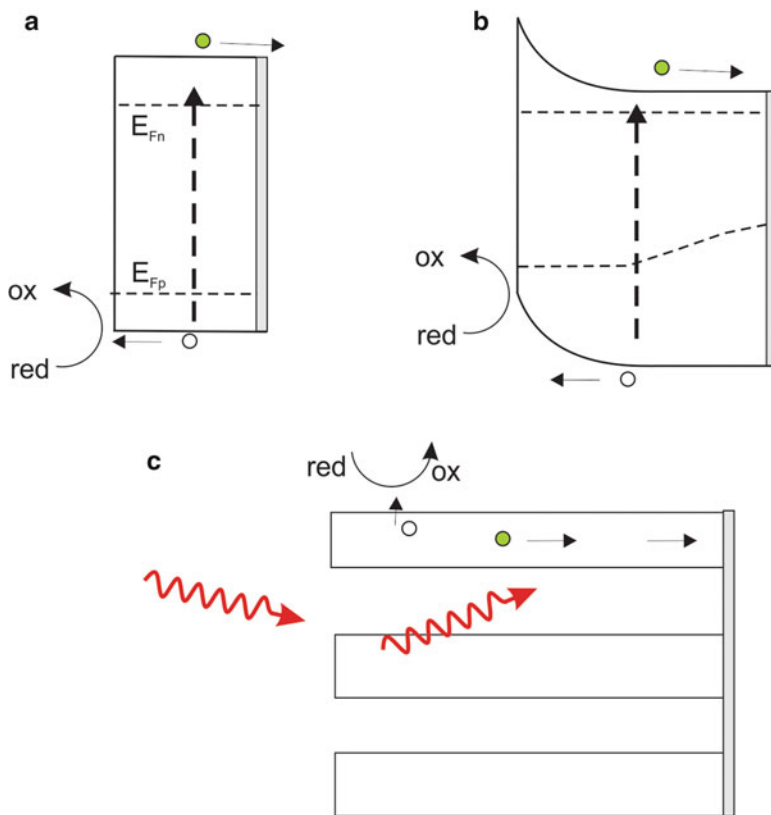
Fig. 6.1 Scheme of the main semiconductor PEC structures for charge generation toward electrochemical reaction. (**a**) Flat nanolayer without internal field distribution. (**b**) Thick semiconductor film with depletion layer at the contact with electrolyte. (**c**) Semiconductor nanostructure permeated with electrolyte and promoting light scattering

The significance of surface states is first discussed in Sect. 6.5. The charge transfer by competition of the direct transfer from conduction band and indirect transfer via surface states, indicated in Fig. 6.2a, will be discussed in Sect. 6.5.2 Then we discuss the effect of surface modification and their characterization by IS in Sects. 6.7 and 6.8.

Finally, Fig. 6.1c shows a morphology representative of a variety of nanoscale porous films that have been widely explored. One evident advantage is the shorter distance of the photogenerated charges to the semiconductor/solution interface, which decreases the needed diffusion length, provided that the complementary carrier can be collected within the central region of nanowires. This model for a nanostructured electrode will be discussed in Sect. 6.8.
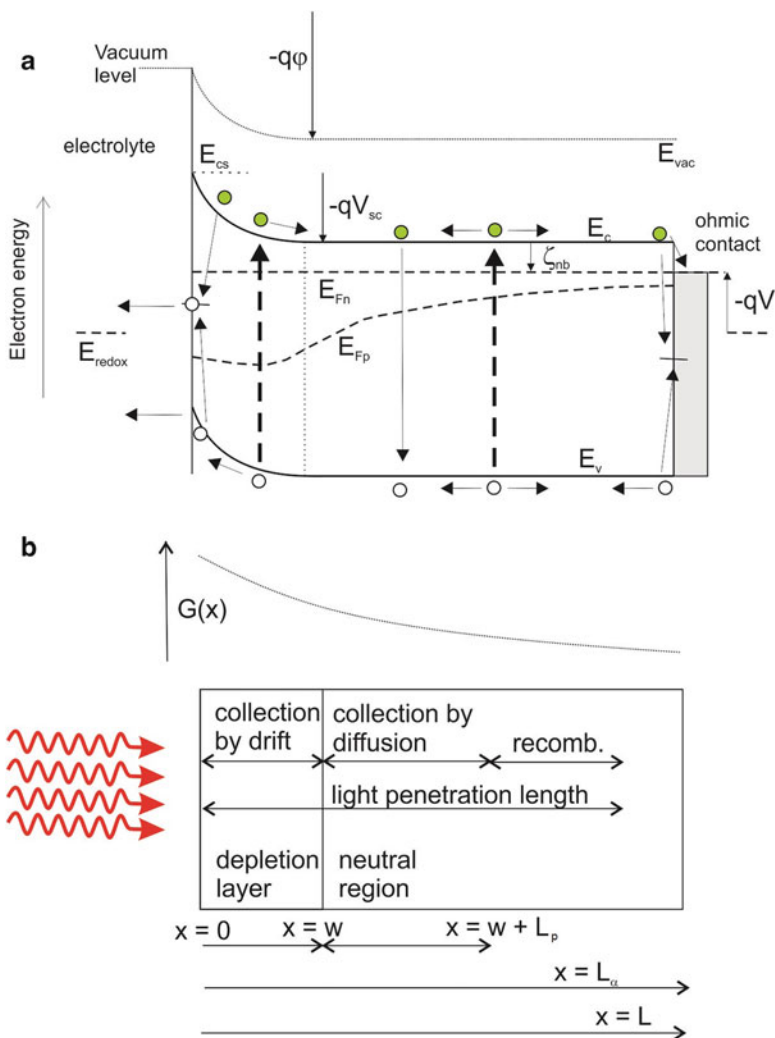
Fig. 6.2 (**a**) Standard representation of energy diagram of a semiconductor electrode. The photogenerated electrons and holes can be extracted at the contacts or recombined in the bulk or at interface. The majority carrier electrons have a flat Fermi level at moderate illumination level. The left contact realizes the useful photoelectrochemical reaction by photogenerated holes from the valence band. Surface states at the semiconductor surface may also contribute to interfacial charge transfer, but they are also a source of recombination by trapping majority carriers. The right contact is an ohmic contact that extracts majority carriers toward a complementary electrode in the PEC. This contact may also be a locus of surface recombination. (**b**) The utilization of photogenerated carriers at the reaction interface requires extraction in depletion region and along one diffusion length of the minority carrier. Carriers generated further away are lost by recombination. On *top* of the diagram is shown the generation profile

6.2 Steady-State Operation of PEC Systems

Let us describe summarily the operation of a PEC semiconductor electrode under variation of voltage and illumination as described in Fig. 6.3. In the dark, we can distinguish the voltage-induced current by either majority or minority carrier injection to electrolyte (possibly by different electrochemical reactions). In an n-type semiconductor electrode, negative current increases at cathodic bias due to injection of majority carriers to the electrolyte. In the dark, the concentration of minority carriers (holes) is rather small; hence, an anodic current only occurs at strong positive bias by hole injection from the substrate, Fig. 6.3a (point 1).

The generation of electron–hole pairs produces a separation of Fermi levels, Fig. 6.3b, and causes an anodic photocurrent as indicated in Fig. 6.3a. Ideally, the photocurrent is added to the dark current that consists of a separate oxidation reaction, as in the dashed line of Fig. 6.3a (point 3). However, strong recombination combined with slow charge transfer may delay the onset of photocurrent to more anodic voltage than the flat band potential, as shown by the dark line in Fig. 6.3a (point 2). This fundamental physical operation of semiconductor electrodes has been well illustrated in the simple model by Peter that compares the initial photo-current after onset illumination with the stable photocurrent that is decreased by the recombining holes, see Sect. 1.3.2. This point will be quantitatively addressed from the perspective of IS in Sect. 6.3. We observe that increased recombination delays the onset of photocurrent to the point 2 in the diagram. The photovoltage, defined in Fig. 1.16, as the point where the current of an illuminated semiconductor electrode is zero, is decreased. There is also a reduction of fill factor, and third feature is a decrease of the steady-state photocurrent that can be fully recovered at more positive potential, when all recombination is suppressed, see point 3 in Fig. 6.3a.

Let us note the significance of improving the three following characteristics of a semiconductor electrode: photovoltage, photocurrent, and fill factor. In the operation of a practical tandem cell, as that shown by Sivula in Fig. 12.2, the operation point for unassisted fuel production is the intersection of anode and cathode current voltage curves, as depicted in Fig. 6.3c. It is therefore very important to achieve a control of the physical, chemical, and material properties that govern the steady-state current voltage curve of a semiconductor applied to fuel production from visible light, in order to enhance the current at the intersection point, that will ultimately determine the conversion efficiency as noted by Smith in Chap. 4. One example of enhancing the PEC operation of a photoanode is shown in Fig. 6.4 (Zhong and Gamelin 2010). The current voltage curves of hematite (Fe_2O_3) undergo a major improvement by deposition of a cobalt–phosphate (Co–Pi) water oxidation catalyst. In Fig. 6.5a, we show the current density–voltage curves of a Fe_2O_3 hematite electrode for water oxidation and $[Fe(CN)_6]^{4-}$ oxidation. The latter is more facile as it is a one-hole transfer reaction by direct transfer from the valence band while the oxygen evolution reaction is a four-hole reaction (see mechanistic details in Chap. 2) that involves the trapping of holes at surface states as discussed later (Klahr et al. 2012a, b, c). One major goal of IS is to contribute to the understanding of the specific processes that cause these significant changes in current voltage curve.
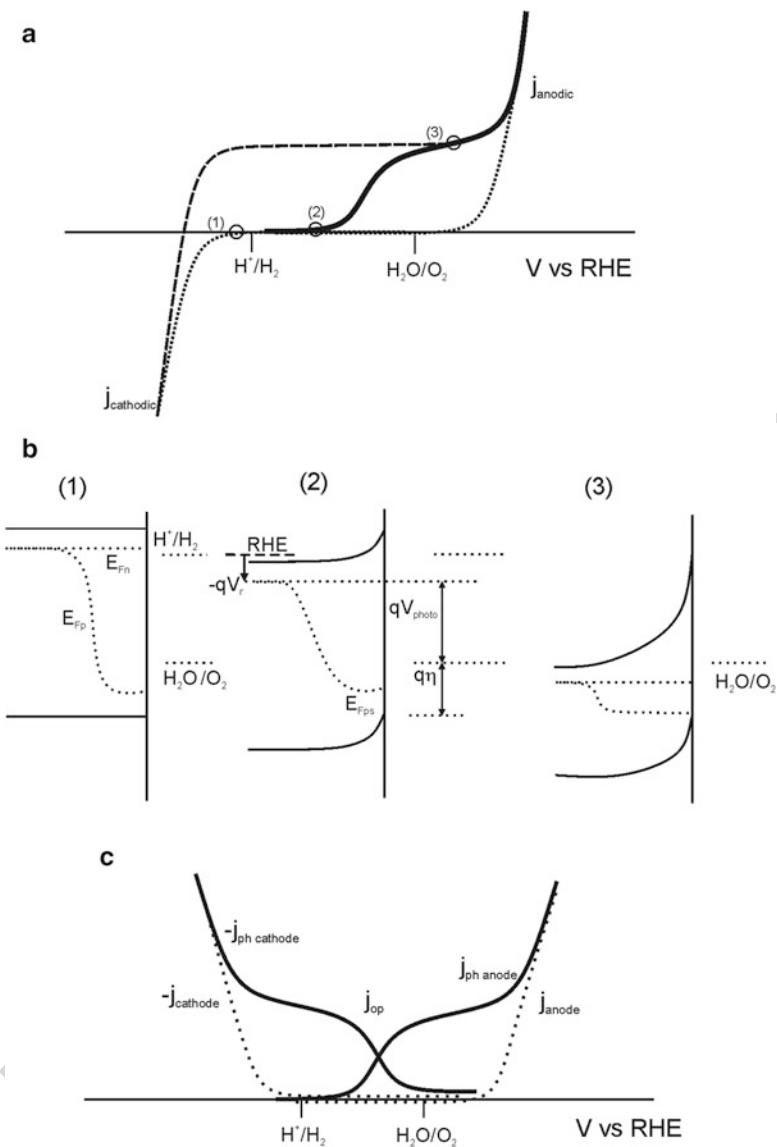
Fig. 6.3 (a) Current density–voltage curves resulting from the PEC operation of a semiconductor photoanode. *Dotted line* is dark current density–voltage curve for the oxygen evolution reaction. *Dashed line* is the idealized curve under illumination. The *solid line curve* is a realistic curve including normal features of semiconductor/electrolyte junction as recombination of electrons and holes. (**b**) Representation of energy diagram of semiconductor/water interface at different voltages vs. RHE. The points *1*, *2*, *3* correspond to the different electrode potentials indicated in (**a**). (**c**) Combination of anode and cathode in a tandem PEC showing the operation point at the intersection between the curves

Fig. 6.4 Dark current (*dotted*) and photocurrent (*solid* and *dashed*) densities of Fe_2O_3 photoanodes before and after 30 min of Co–Pi deposition, measured in pH 13.6 NaOH (**a**) and pH 8 KPi (**b**) at 50 (*thick line*) and 10 mV/s (*dashed line*). The α-Fe_2O_3 data (*red curves*) were collected at 10 mV/s. The *circles* denote steady-state photocurrent densities after 200 s of continuous illumination under 1 sun, AM 1.5 simulated sunlight. Reproduced with permission from Zhong and Gamelin (2010)
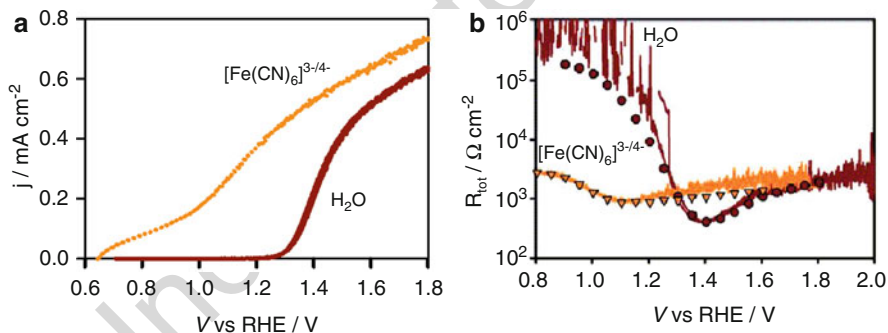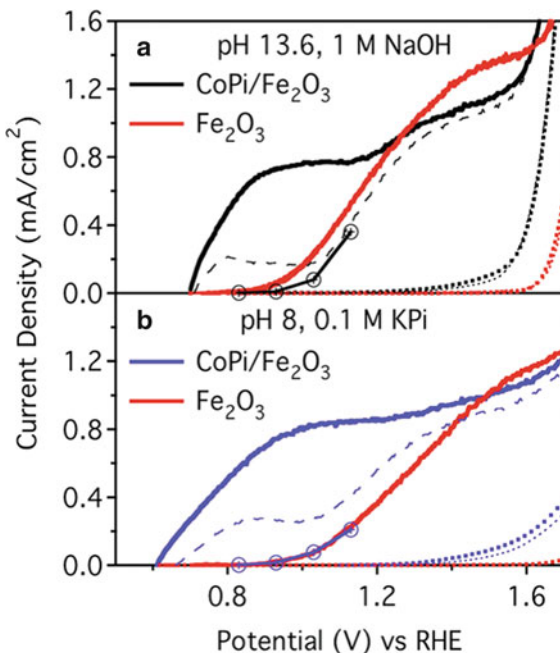
Fig. 6.5 (**a**) jV curve of a hematite electrode in contact with a H_2O and $[Fe(CN)_6]^{3-/4-}$ electrolyte under 1 sun illumination. (**b**) Total (dc) resistance calculated from dV/dj of the jV curves (*lines*) and from IS data (*symbols*) for H_2O and $[Fe(CN)_6]^{3-/4-}$ electrolytes. Reproduced with permission from Klahr et al. (2012a)

6.3 Resistances and Capacitances in PEC Systems

Basically, IS provides a decomposition of the electrical response of the sample into resistances and capacitances, and the rationale for this technique is the following. IS consists of the measurement of the ac electrical current $\hat{I}(\omega)$ at a certain angular

134 frequency ω, when ac voltage $\widehat{V}(\omega)$ is applied to the system, or vice versa,
135 measurement of $\widehat{V}(\omega)$ at applied $\hat{I}(\omega)$. The impedance is:

$$Z(\omega) = \frac{\widehat{V}(\omega)}{\hat{I}(\omega)} \qquad (6.1)$$

136   The symbol $\hat{x}$ over a quantity x indicates that $\hat{x}$ has the following properties. It is
137 the complex amplitude of a sinusoidal (ac) perturbation of x and it is a small
138 perturbation. The "smallness" of $\hat{x}$ is required in order to obtain in Eq. (6.1) the
139 *linear* impedance, i.e., $\hat{I}(\omega)$ is linear with respect to $\widehat{V}(\omega)$, or vice versa, so that $Z(\omega)$
140 is independent of the amplitude of the perturbation. More generally, the relationship
141 between input and output is a *transfer function*. Another example of this method
142 which resorts to transfer functions is Intensity Modulated Photocurrent Spectros-
143 copy (IMPS), which determines the photocurrent response to modulated illumina-
144 tion of a semiconductor electrode, see for instance Li and Peter (1985).
145   Provided that the PEC operation is stable, the analysis of the frequency domain
146 response can be realized at each point of the steady-state curve as that shown in
147 Fig. 6.3a, that is the truly stationary value of current for each voltage in the required
148 condition of illumination, electrolyte, etc. The important property of IS is that we
149 obtain a spectroscopy at each point by virtue of the frequency variation. Examples
150 shown in Fig. 6.6 correspond to the conditions of Fig. 6.5. It is observed that IS
151 provides different features consisting either of one or two arcs. The interpretation of
152 these features is the key to reveal specific kinetic and charge storage properties in
153 the water splitting process. The information contained in the experimental mea-
154 surements of impedance spectroscopy and represented in the complex plane imped-
155 ance plots must be analyzed in terms of a suitable equivalent circuit (EC), in order
156 to extract the capacitances and resistances, which are related to the basic electronic
157 processes of charge accumulation, recombination, and charge transfer.
158   The resistances are associated to different processes of carrier flux, either inside
159 semiconductor materials or at interfaces. These phenomena can be included in a
160 physicochemical model based on transport and conservation equations, as
161 discussed later, and solved for a small perturbation condition to give the impedance
162 model. In the analytical model, in-phase components provide resistances and out-
163 of-phase components of the current provide capacitances. The capacitances repre-
164 sent a charge storage mechanism and they can be divided into two main kinds, as
165 further discussed in the textbook by Bisquert (2014). Dielectric capacitances are
166 associated to an internal electrical field that is produced by spatial charge separation.
167 Chemical capacitance is due to the variation of chemical potential, or carrier
168 concentration, in one type of electronic state. The identification of the capacitances,
169 as well as the resistances, usually proceeds by adapting the data gathered at different
170 voltages to a single EC. The progression of capacitances and resistances along the
171 voltage variations gives valuable information about the meaning of each element and
172 the overall behavior of the system.

Fig. 6.6 Complex plane impedance plots for IS data measured under 1 sun illumination for H_2O (*circles*) and [Fe $(CN)_6]^{3-/4-}$ (*triangles*) electrolytes at (**a**) 1.3 V vs. RHE and (**b**) 1.6 V vs. RHE. Reproduced with permission from Klahr et al. (2012a)
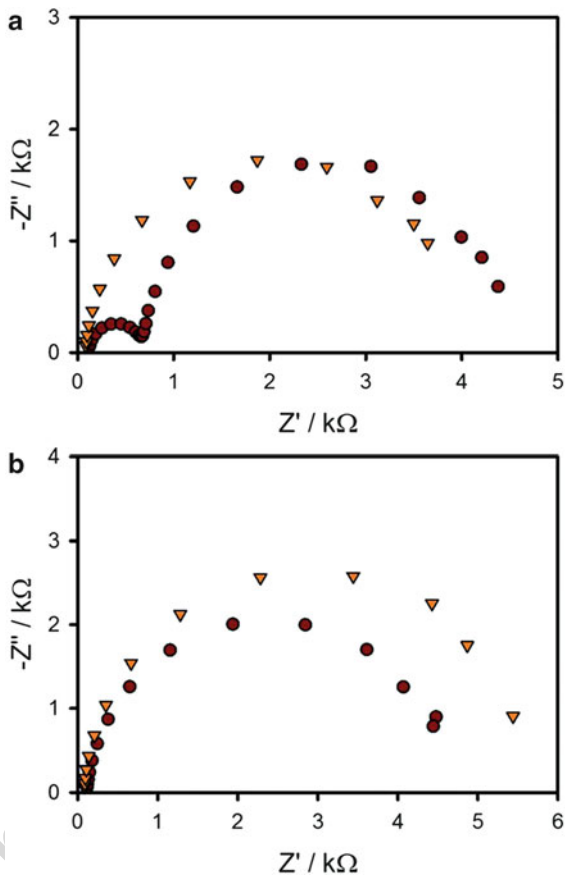
In practice, the photoelectrode response is composed of different charge sepa- 173
ration and charge injection steps. The analysis of some of these processes by IS has 174
been well described in previous publications for related systems (Bisquert 2002, 175
2008; Bisquert and Fabregat-Santiago 2010; Fabregat-Santiago et al. 2011). Some 176
of these processes are shown in Fig. 6.2a, and we can observe that we have diffusion 177
along the bulk material, trapping and detrapping at the surface, interfacial charge 178
transfer, etc.. . . Correspondingly, we will obtain transport resistance in the bulk and 179
interfacial resistances associated to trapping in surface and charge transfer. Espe- 180
cially in the case of slow electrocatalytic reaction like the multistep oxygen 181
evolution reaction, the characterization of the interfacial charge transfer is a 182
challenging topic as discussed in Chap. 2 by Doyle. One particularly important 183
aspect of IS of PEC system is an understanding of the *charge transfer resistance* R_{ct} 184
that is associated in a general sense to the interfacial charge transfer steps of the 185
electrochemical reaction. Monitoring the charge transfer resistance can provide 186
information about the charge transfer rate for electrochemical reactions. This 187
charge transfer resistance must be deconvoluted from the total resistance of the 188

189 system provided that the adequate equivalent circuit conveying the relevant infor-
190 mation of the operating physicochemical processes is used. This deconvolution
191 process is possible by virtue of the capacitive response of the electrodes.

192   In one simple example, let us consider a photoelectrode in contact with an
193 electrolyte solution. If the traffic of carriers from the back contact to the solution
194 consists of two serial processes $R_{tot} = R_1 + R_{ct}$, R_1 accounting for charge transport,
195 and R_{ct} for interfacial charge transfer, the capacitance allows separation of these
196 additive resistances. Considering the classical Randles circuit (as the one shown in
197 Fig. 6.13c), the surface capacitance is associated with the Helmholtz layer at the
198 electrode/solution interface, C_H, and only affects the parallel resistance R_{ct}.

199 6.4 Total Resistance R_{dc} and the Connection to jV Curves

200 As mentioned, one quantity of central interest in the analysis of PEC systems is the
201 total or dc resistance R_{dc}. This resistance can be obtained by removing all capacitors
202 in the EC, and it holds a special relationship to the jV curve. Let us choose a certain
203 point of bias voltage V_0 with the associated current density j_0. At this point, a small
204 displacement of voltage $\widehat{V}(\omega = 0)$ implies a change of current $\hat{j}(\omega = 0)$. The value
205 $\omega = 0$ in parenthesis indicates that the displacement is arbitrarily slow, i.e., $\widehat{V}(0)$
206 and $\hat{j}(0)$ attain a value that is independent of time, i.e., the steady-state value. Since
207 the resistance in IS is related to change of electrical current with respect to change
208 of voltage, the resistance is associated to a derivative of a carrier flux with respect to
209 a generalized voltage. For an electrode with macroscopic area A, the quotient of the
210 small quantities gives

$$Z(0) = \frac{\widehat{V}(0)}{A\hat{j}(0)} \tag{6.2}$$

211   Therefore, we obtain a resistance $Z(0) = R_{dc}$ given by

$$R_{dc} = \left(A\frac{\partial j}{\partial V}\right)^{-1} \tag{6.3}$$

212   The dc resistance of the photoelectrode R_{dc} (per unit area) is the reciprocal of the
213 slope of the jV curve. Figure 6.5b compares the dc resistance measured by IS with
214 the effective resistance obtained as a reciprocal derivative indicated in Eq. (6.3). It
215 is clearly observed that both approaches are in good agreement, which establishes
216 the connection between the two types of measurements.

217   Let us further discuss the meaning of R_{dc} features observed in water splitting
218 PEC systems. We adopt the simple model of Reichman (1980) to describe the effect
219 of internal recombination on jV curves, which was qualitatively discussed in
220 Fig. 6.3a. This model uses the standard assumption that the voltage V applied to

the semiconductor electrode modifies the size of space charge region. The model   221
introduces a kinetic limitation to the extraction of minority carriers to the fuel   222
production reaction. The hole extraction current density is given by the expression   223

$$j = qS_p(p_s - p_{s0}) \tag{6.4}$$

Here, q is the elementary charge, p_s is the concentration of holes at the surface,   224
and parameter S_p is similar to a hole surface recombination velocity. The current is   225
found by a combination of unity collection efficiency in the SCR, and by the   226
solution of diffusion–recombination equation in the neutral region. Neglecting   227
recombination in SCR, the current as function of voltage has the form   228

$$j = \frac{j_{ph} - j_0 e^{-qV/k_B T}}{1 + \frac{j_0}{j_{s0}} e^{-qV/k_B T}} \tag{6.5}$$

Here, j_{ph} is the photocurrent given by Gärtner's model, j_0 is the reverse saturation   229
current, and $j_{s0} = -qS_p p_{s0}$ is the charge transfer current in equilibrium. The   230
resistance is given by the form   231

$$R_{ct}^{-1} = \frac{j_0 q}{k_B T} \left(1 + \frac{j_{ph}}{j_{s0}}\right) \frac{e^{-qV/k_B T}}{\left(1 + \frac{j_0}{j_{s0}} e^{-qV/k_B T}\right)^2} \tag{6.6}$$

In Fig. 6.7a, we show the current density–voltage curve for different values of   232
the extraction parameter S_p. First we note that if the extraction velocity is infinite,   233
then the jV curve is similar to a diode curve   234

$$j = j_{ph} - j_0 e^{-qV/k_B T} \tag{6.7}$$

This behavior corresponds to the dashed curve in Fig. 6.3a and the plain line in   235
Fig. 6.7a. In this idealized model, the total resistance is an exponential function with   236
no minimum feature, as shown in Fig. 6.7b. When the transfer of holes has some   237
limitation, recombination in the neutral region is favored near the flat band poten-   238
tial, and the photovoltage is displaced to lower values. In this case, a minimum of   239
the resistance is observed. Consequently, the presence of a minimum in the total   240
resistance indicates sluggish carrier extraction.   241
    We remark that in the IS analysis of the model of Reichman (1980), the   242
limitation to charge transfer, observed in the jV curve, is a combination of two   243
factors: sluggish charge transfer and internal recombination. However, the model in   244
Eq. (6.5) is a simplification with respect to recombination in the space charge region   245
and other features. In order to establish the properties of the charge transfer   246
resistance in a more general setting, we have developed extensive simulations of   247
the semiconductor electrode model system indicated in Fig. 6.2, as described in the   248
paper (Shi et al. 2016). The system is analyzed considering photogenerated   249
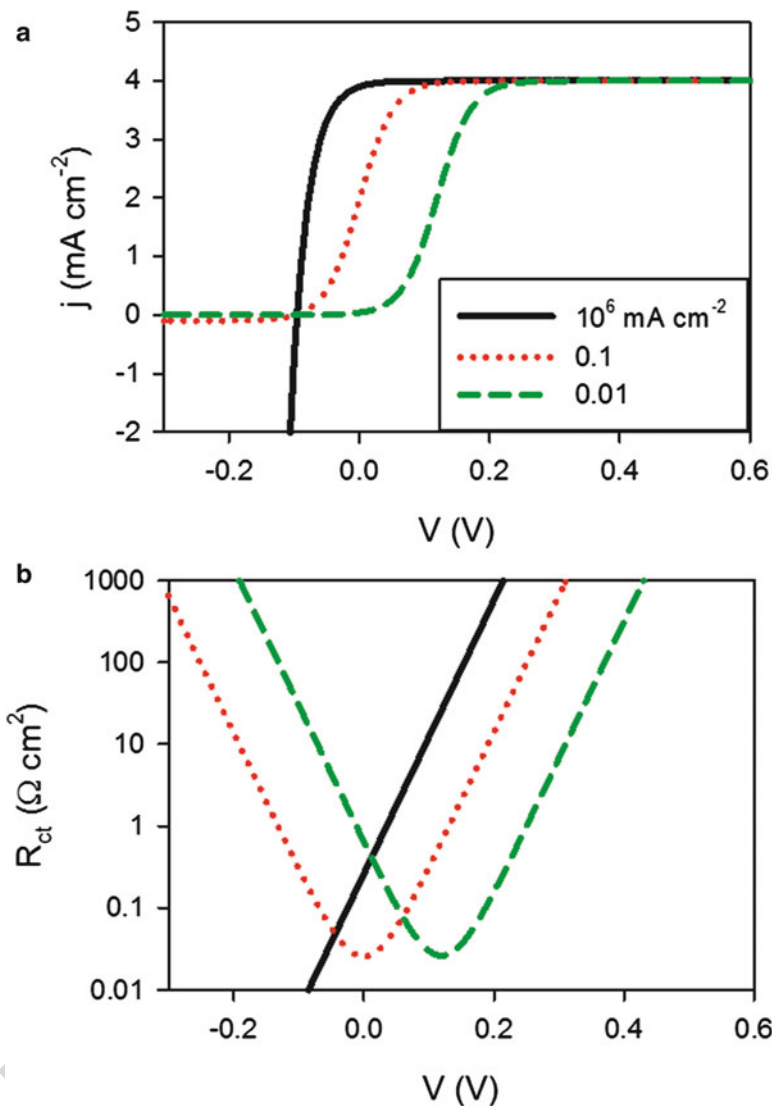
Fig. 6.7 Current voltage curve of a photoanode (**a**) and charge transfer resistance (**b**) in the model of Reichman with limitation to extraction of the minority carrier at the semiconductor/electrolyte interface. The photocurrent is $j_{ph} = 4$ mA/cm^2, the reverse saturation current is $j_0 = 0.1$ mA/cm^2, and the hole charge transfer current j_{s0} is indicated in the *inset panel*

250   electrons and holes with densities n and p per unit volume at a rate
251    $G = \alpha\Phi_0\exp(-\alpha x)$, being α the optical absorption coefficient, and Φ_0 the photon
252   flux, transport by drift and diffusion, and the formation of electrical fields including
253   band bending at SCR according to Poisson equation. We also incorporate different
254   rates or charge extraction at either contact. Recombination can occur either in bulk,
255   according to the expression,

$$U_r = B(np - n_0 p_0) \tag{6.8}$$

or at the surface, as indicated in Eq. (6.4) for minority carriers. The corresponding   256
expression for majority carrier electrons at the back contact is: 257

$$j = qS_n(n_s - n_{s0}) \tag{6.9}$$

Several jV curves obtained in this modeling are shown in Fig. 6.8a, according to   258
different rates of surface or bulk recombination. Again we note how the resistance   259
of the system reaches a minimum, Fig. 6.8b, which corresponds to the inflection point   260
in the jV curve according to Eq. (6.3). The effect of increasing the surface recombi-   261
nation, via the parameter S_n, is to displace the minimum of the resistance toward   262
cathodic potentials while for slower bulk recombination, tuned via the parameter B,   263
this minimum is decreased and is associated to enhanced charge transfer   264
kinetics.   265

Here, we should remark that R_{dc} is not just a charge transfer (interfacial) quantity   266
but it is influenced by recombination and diffusion events that occur far in the bulk.   267
However, if those elements are not coupled to significant capacitive elements, then   268
the total resistance couples to a single capacitance and the impedance gives a single   269
arc feature as shown in Fig. 6.6b. The situation is different when we observe   270

Fig. 6.8 (**a**) jV curves and (**b**) Charge transfer resistance for different values of the bulk recombination (B) and surface recombination at the electron selective contact (S_n). The values of the recombination rates are $B = 10^{-8}$ cm^3/s and $S_n = 10^{-2}$ cm/s (*blue line*), $B = 10^{-7}$ cm^3/s and $S_n = 10^{-2}$ cm/s (*red line*) and $B = 10^{-7}$ cm^3/s and $S_n = 10^{-4}$ cm/s (*black line*). Reproduced with permission from Shi et al. (2016)
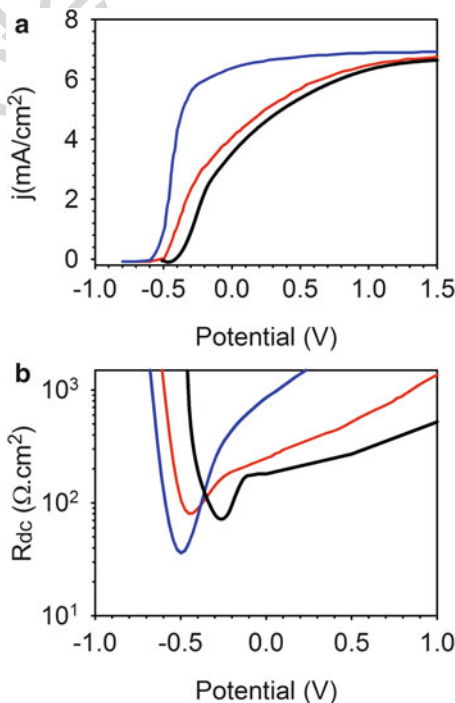
271 transmission line features as commented later on in Sect. 6.7, as then the ac
272 measurement resolves the variation of recombination and diffusion resistances
273 across the sample thickness (Bisquert 2002; Wang et al. 2006).

6.5   Charge Transfer via Surface States

6.5.1   Properties of Surface States

276 At the surface of a crystalline semiconductor material, the periodic crystal symme-
277 try is broken and consequently, there exist electronic states within the bandgap,
278 which are termed surface states. These surface states can be intrinsic to the
279 semiconductor surface or extrinsic when their existence depends on the environ-
280 mental conditions of the semiconductor (presence of adsorbates or electrolytes in
281 contact with the semiconductor surface). In the context of semiconductor electro-
282 chemistry, surface states play a key role on the kinetics of interfacial reactions at
283 illuminated electrodes. Particularly, the importance of surface states for the kinetics
284 of electrochemical reactions involving minority carriers has been highlighted from
285 the early studies on III–V semiconductors (Kelly and Memming 1982) and Fe_2O_3
286 (Dareedwards et al. 1983). More recent results in relation to IS have been summa-
287 rized by Bertoluzzi et al. (2016). Such states can act as recombination centers for
288 minority carriers generated by light; and consequently, surface recombination
289 competes effectively with charge transfer from the semiconductor bands. Charge
290 localization in surface states also leads to considerable changes in the Helmholtz
291 potential that result from trapping, accounting for the magnitude of the
292 overpotentials with respect to the flat band potential (V_{fb}) required for the onset
293 of photocurrent. This topic will be discussed in Sect. 6.6.
294   Impedance spectroscopy allows probing the density of surface states by moni-
295 toring the surface state chemical capacitance (C_μ^{ss}) as a function of the applied bias
296 (electron Fermi level). In dark condition, majority carriers are in equilibrium with
297 the transport band (conduction band for an n-type material) and this capacitance is
298 termed the equilibrium chemical capacitance of surface states, $C_{\mu eq}^{ss}$, defined as
299 (Bisquert 2014):

$$
\begin{aligned}
C_{\mu eq}^{ss} &= Aq^2 N_{ss} \frac{\partial f_{ss}}{\partial E_{Fn}} \\
&= A \frac{q^2 N_{ss}}{k_B T} f_{ss}(1 - f_{ss})
\end{aligned}
\tag{6.10}
$$

300 N_{ss} is the density of surface states, f_{ss} the fractional occupancy of the states, k_B the
301 Boltzmann constant, and E_{Fn} the electron Fermi level. In the presence of a wide
302 distribution of surface states such as the Gaussian distribution, the surface state
303 capacitance is related to the density of surface states (DOS), $g_{ss}(E)$, as

$$C_{\mu\text{eq}}^{\text{ss}} = A_s q g_{\text{ss}}(E_{\text{Fn}}) \tag{6.11}$$

As an illustrative example, Fig. 6.16, discussed later on, shows the DOS of 304
hematite (α-Fe$_2$O$_3$) in contact with an aqueous solution under illumination at two 305
different pH conditions. 306

6.5.2 Theory of Charge Transfer via Surface States   307
and Valence or Conduction Band   308

Under illumination of a photoanode, the valence band obtains abundant excess of 309
minority carriers, holes, which can be transferred to the species in solution by a 310
direct charge transfer mechanism in order to launch the fuel production reaction. 311
But in the presence of surface states, these localized bandgap states may capture 312
hole carriers and consequently present another favorable pathway for indirect 313
charge transfer as well as a new undesirable recombination pathway, as indicated 314
in Fig. 6.2a (Salvador and Gutierrez 1984; Salvador and Gutiérrez 1984). The solar 315
to chemical energy conversion efficiency strongly relies on the magnitude of both 316
processes and it is therefore primordial to differentiate between each one of them. 317
In particular, efficient solar fuel production requires reduction of the effect of 318
surface state-assisted recombination at low applied bias. 319
    In order to understand the effect of the competing surface state-assisted recom- 320
bination and indirect charge transfer processes on water oxidation, we consider a 321
first simple kinetic model that neglects any electrostatic influence such as the 322
presence of an electric field. Such model is depicted in Fig. 6.9a (Bertoluzzi and 323
Bisquert 2012). At low bias, direct charge transfer of holes from the valence band 324
can be neglected and only three processes occur at this interface: trapping/ 325
detrapping of holes, charge transfer of holes, and trapping/detrapping of electrons. 326
Note that the detrapping kinetic constant is directly proportional to the trapping 327
constant through the detailed balance principle (Bisquert 2010). Hence, it is equiv- 328
alent to refer to either trapping or detrapping kinetics indistinctly. 329
   From this simple picture, it is clear that surface state-assisted recombination and 330
hole transfer to the solution have a common factor, which is hole trapping/ 331
detrapping. In fact, Fig. 6.10 shows that the effect of trapping/detrapping does not 332
influence notably photoelectrochemical performances of a photoanode at low 333
applied bias. On the contrary, it is the ratio between the detrapping of electrons 334
and the charge transfer kinetic constant (ε_n/k_s) which determines the relative 335
importance of both competing processes and the onset voltage of the photo- 336
oxidation reaction. In particular, the lesser the ratio ε_n/k_s, the smaller the onset 337
voltage. It is therefore necessary to probe the evolution of this quantity when 338
resorting to surface treatments such as passivating layers or catalysts. 339
    In order to obtain a more detailed view of charge transfer processes with 340
electrostatic features, in steady-state conditions, we have used the general 341
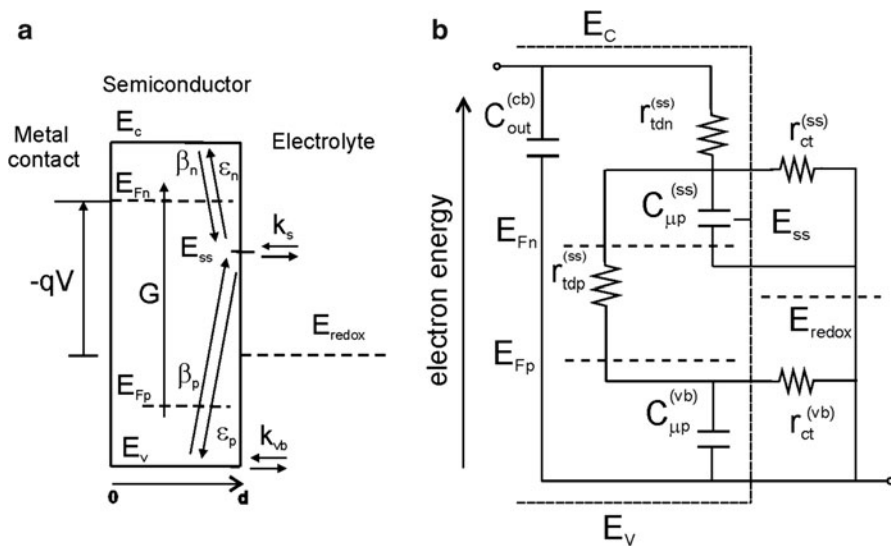
Fig. 6.9 (**a**) Scheme of the kinetics of the processes occurring at the semiconductor/solution interface: generation of electrons and holes at a rate G, trapping of electrons from the conduction band (kinetic constant β_n) and detrapping (ε_n). Trapping of holes from the valence band (β_p) and detrapping (ε_p). Charge transfer of holes from the surface states (k_s) and from the valence band (k_{vb}). (**b**) Equivalent circuit obtained from a small ac perturbation. C_{out}^{cb} is the semiconductor capacitance, $C_{\mu p}^{ss}$ is the traps chemical capacitance, $C_{\mu p}^{vb}$ the valence band chemical capacitance, r_{tdn}^{ss} the trapping/detrapping resistance of electrons from the conduction band, r_{tdp}^{ss} the trapping/detrapping resistance of holes from the valence band, r_{ct}^{ss} is the charge transfer resistance from the traps and r_{ct}^{vb} holes transfer resistance from the valence band. Reproduced with permission from Bertoluzzi and Bisquert (2012)

342 simulation procedure described in Sect. 6.4 to obtain some insight into the compe-
343 tition of charge transfer pathways (Bertoluzzi et al. 2016). In Fig. 6.11, we present
344 simulations of current voltage characteristics and the corresponding evolution of
345 the hole density in the valence band at the semiconductor/electrolyte interface. In
346 plot 1 of Fig. 6.11a, one can appreciate the effect of direct charge transfer of holes
347 from the valence band on the photoelectrochemical performance of a photoanode.
348 The first feature that can be observed is a very small photocurrent at low applied
349 bias, which arises from strong electron–hole recombination. Once the onset voltage
350 is reached, the space charge region sustains a sufficient electric field in order to
351 counterbalance recombination so that charge separation is favored and the anodic
352 photocurrent increases, see Fig. 6.3b. Finally, as the applied voltage increases, the
353 anodic photocurrent reaches saturation, whose value can be approximated within
354 the framework of the model of Reichman (1980), as discussed earlier. This
355 approach has been reported and discussed in several publications, and for more
356 information on this topic, the reader is referred to a detailed review by Cendula
357 et al. (2014).
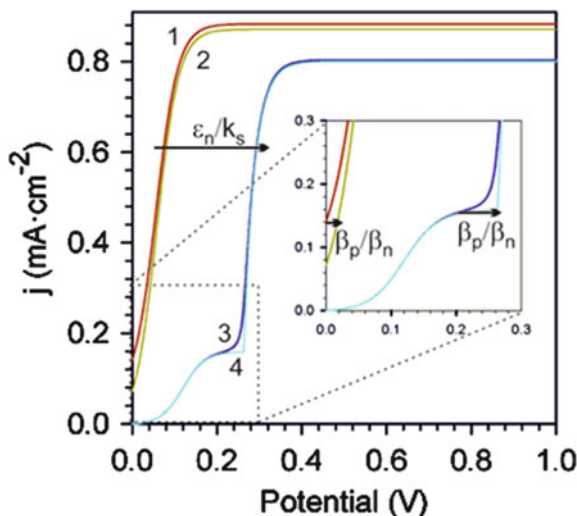
Fig. 6.10 *jV* curves for different cases of the kinetic model including the electron trapping/detrapping, hole transfer from the surface states, and hole trapping/detrapping. Model parameters are $d = 10\,\text{nm}$, $G = \alpha\phi_0\exp(-\alpha x)$, $\alpha^{-1} = 100$ nm, $\phi_0 = 5 \times 10^{16}\,\text{cm}^{-2}\,\text{s}^{-1}$, $k_B T = 26\,\text{meV}$, $E_c = 0\,\text{eV}$, $E_{ss} = -0.12\,\text{eV}$, $N_c = 10^{20}\,\text{cm}^{-3}$, $N_{ss} = 10^{21}\,\text{cm}^{-3}$, and $k_{vb} = 10^{-1}\,\text{s}^{-1}$, (*1*) $\varepsilon_n = 10^{-1}k_s = 1\,\text{s}^{-1}$, $\beta_p = 10^{-3}\beta_n = 10^{-21}\,\text{cm}^3/\text{s}$, (*2*) $\varepsilon_n = 10^{-1}k_s = 1\,\text{s}^{-1}$, $\beta_p = 10^3\beta_n = 10^{-15}\,\text{cm}^3\,\text{s}^{-1}$, (*3*) $\varepsilon_n = 10^3 k_s = 10^3\,\text{s}^{-1}$, $\beta_p = 10^{-3}\beta_n = 10^{-18}\,\text{cm}^3/\text{s}$, (*4*) $\varepsilon_n = 10^3 k_s = 10^3\,\text{s}^{-1}$, $\beta_p = 10^3\beta_n = 10^{-12}\,\text{cm}^3/\text{s}$. Reproduced with permission from Bertoluzzi and Bisquert (2012)

For indirect charge transfer (plot 2 of Fig. 6.11a), the photogenerated holes are 358 trapped in surface states and can subsequently oxidize water or recombine with 359 trapped electrons. When a positive bias of sufficient magnitude is applied, surface 360 states are filled with holes and hole transfer reaches a maximum; this is when anodic 361 current reaches a first plateau, as indicated by the gray dashed lines of Fig. 6.11a 362 (plot 3). After saturating surface states with holes, the population of holes in the 363 valence band starts increasing. The photoanodic current subsequently keeps on 364 increasing and saturates once the surface state-assisted recombination has been 365 totally eliminated by the withdrawal of electrons from the surface. In principle, if 366 surface state-assisted recombination is much smaller than photogenerated hole 367 transfer, the maximum achievable anodic current can be higher than the 368 photogenerated current with surface states compared to the situation without 369 surface states, as observed in Fig. 6.11a. Once again, the discrimination between 370 both competing processes is fundamental in the characterization of water splitting 371 devices and determining the ratio ε_n/k_s, previously mentioned appears to be pri- 372 mordial in order to optimize the photocurrent of these devices. 373

The ratio ε_n/k_s can be obtained by impedance spectroscopy. For a quantitative 374 calculation of impedance spectroscopy expression and equivalent circuit involving the 375 direct and indirect charge transfer pathways, the model of Fig. 6.9a has been utilized 376 (Bertoluzzi and Bisquert 2012). This model provides the full equivalent circuit of 377
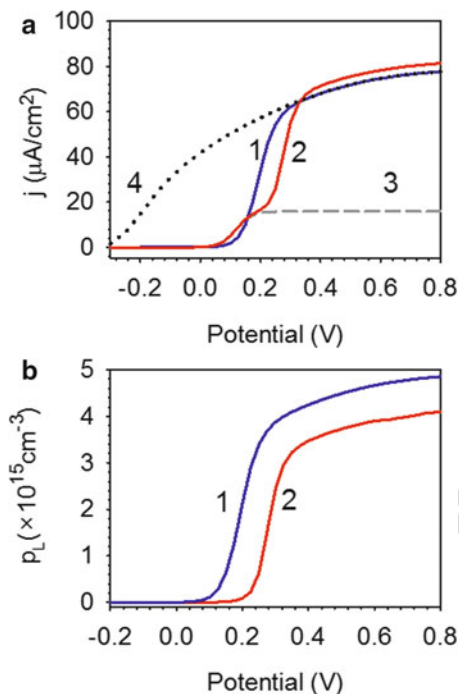
Fig. 6.11 (**a**) Full drift-diffusion simulations of the current voltage plots when holes are directly transferred from the valence band (*1*) and when direct hole transfer competes with indirect charge transfer from the surface states (*2*). The current associated to hole transfer from the traps, in the framework of this latter model, is represented in *gray dashed lines* (*3*). We also indicate the *jV* curve for a perfect hole selective contact without surface states (*4*). (**b**) Corresponding hole density in the valence band at the semiconductor/electrolyte interface as a function of the applied voltage. Reproduced with permission from Bertoluzzi et al. (2016)

378 Fig. 6.9b that contains a large number of features. It is important to remark that this
379 general equivalent circuit for a photoanode contains three types of capacitances:

380 1. The outer capacitance termed $C_{\mathrm{out}}^{\mathrm{cb}}$ describes the coupling of majority carriers
381   (electrons in this case) to the external current collector. This capacitance directly
382   responds to applied bias voltage. In a more general spatial model as that of
383   Fig. 6.2, this outer capacitance must include the electrostatic capacitances,
384   namely, the semiconductor capacitance due to the depletion layer C^{sc} and the
385   Helmholtz capacitance.
386 2. The capacitance of surface states has been already discussed in Sect. 6.5.1.
387   However, it is important to stress that this capacitance, which we note $C_{\mu\mathrm{p}}^{\mathrm{ss}}$, is
388   different from the one measured in dark and presented in Sect. 6.5.1 ($C_{\mu\mathrm{eq}}^{\mathrm{ss}}$). In
389   fact, in this case, the variation of the occupation probability of surface states, f_{ss},
390   is not only affected by the trapping of majority carriers but also by the
391   photogenerated minorities. The resulting expression for $C_{\mu\mathrm{p}}^{\mathrm{ss}}$ is consequently
392   more complex (Bertoluzzi and Bisquert 2012).

3. The valence band holes capacitance $C_{\mu p}^{vb}$, explicitly depends on the chemical capacitance of the traps (Bertoluzzi and Bisquert 2012). This is due to the fact that holes in the valence band are not connected to any of the external Fermi levels, neither the Fermi level of the metal contact nor the redox level in solution. Therefore, charge in capacitor $C_{\mu p}^{vb}$ cannot be directly modulated by external bias. This latter statement has important consequences in terms of IS measurements. In fact, one necessary condition to observe the valence band capacitance is that it must be connected indirectly, via recombination, to the Fermi level of electrons. In absence of recombination, such capacitance could not be measured.

In summary, the EC in Fig. 6.9b models the kinetics of both, electrons and holes surface state-assisted recombination and charge transfer at the interface semiconductor/electrolyte in dynamic regime. This circuit explicitly includes the *three* chemical capacitances that are associated to the separate modes of carrier storage in this system: the conduction band, the valence band, and the surface states. In consequence, this model predicts the observation of three arcs in the complex impedance plot, as shown in Fig. 6.12.

However, the wide bandgap semiconductors usually used for solar fuel production do not allow for the observation of three semicircles in the complex plane. Instead, a maximum of two semicircles is generally observed, as shown in Fig. 6.6, and no more
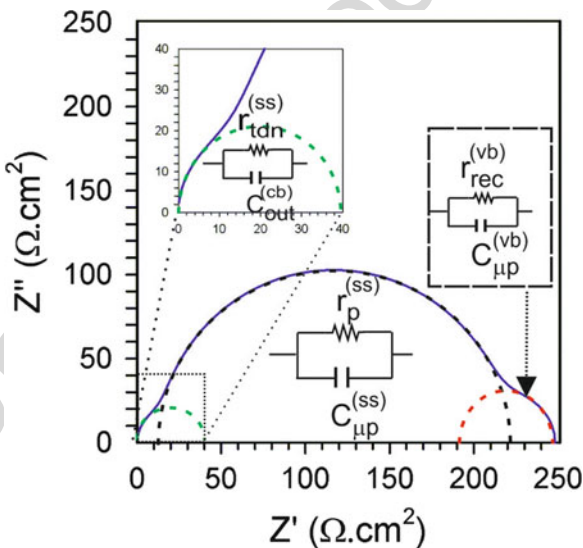
Fig. 6.12 Illustration of the impedance in the complex plane presenting three semicircles. The first semicircle at low frequency corresponds to the valence band charge transfer, the second one to the surface states charge transfer, and the last one at higher frequencies corresponds to the electrons trapping/detrapping. The parameters used for this simulation are: $d = 10\,\text{nm}$, $\alpha^{-1} = 100\,\text{nm}$, $\phi_0 = 5 \times 10^{16}\,\text{cm}^{-2}\,\text{s}^{-1}$, $k_B T = 26\,\text{meV}$, $E_c = 0\,\text{eV}$, $E_{ss} = 0\,\text{eV}$, $N_c = 10^{20}\,\text{cm}^{-3}$, $N_{ss} = 2 \times 10^{21}\,\text{cm}^{-3}$, $k_{vb} = 0.7\,\text{s}^{-1}$, $\varepsilon_n = 10\,k_s = 100\,\text{s}^{-1}$, $\beta_p = 2 \times 10^{-3}\beta_n = 2 \times 10^{-21}\,\text{cm}^3\,/\text{s}$. Reproduced with permission from Bertoluzzi and Bisquert (2012)

412 than two resistance and capacitance values can consequently be extracted from IS
413 measurements. The extraction of these latter elements and their adequate physical
414 interpretation relies on the proper choice of EC. In the following, we discuss a number
415 of approaches that have been found useful in the analysis of experimental data.

416 Figure 6.13 shows different convenient simplifications of the kinetic model and
417 EC of Fig. 6.9 as well as the relevant resistances which can be extracted from the IS
418 data. Figure 6.13a is for the direct charge transfer mechanism without surface
419 states. From this EC, we can extract values for two capacitances and resistances,
420 which are associated to the conduction and valence band carriers. In particular, the
421 low frequency capacitance is associated to hole storage in the valence band.
422 Secondly, the EC of Fig. 6.13b corresponds to the classical EC for the trapping/
423 detrapping and charge transfer of the majority carrier (Hens 1999; Bisquert 2010).
424 This circuit allows extracting values for two resistances and two capacitances,
425 which are associated with the conduction band and surface states. In this circuit,
426 the low frequency capacitance is associated to hole storage in surface states. The
427 EC of Fig. 6.13b has been employed to model the indirect hole transfer for water
428 oxidation with Fe_2O_3 (Klahr et al. 2012a, b, c). Note that in this configuration, it is
429 unfeasible to probe the hole population and consequently extract the recombination
430 resistance associated to electron–hole recombination in the surface states. For the
431 latter purpose, other techniques are needed, such as IMPS (Ponomarev and Peter
432 1995) where light intensity modulations allow to directly vary and probe the hole
433 concentration in the valence band. However, it is worth noticing that the ratio
434 between the electron trapping/detrapping resistance R_{tdn}^{ss} and the charge transfer
435 resistance from the surface states R_{ct}^{ss} is directly related to the ratio ε_n/k_s previously
436 mentioned. Indeed, it can be shown that:

$$\frac{R_{ct}^{ss}}{R_{tdn}^{ss}} = \frac{\varepsilon_n + \beta_n n}{k_s} \tag{6.12}$$

437 At reverse bias, $n \to 0$ and Eq. (6.12) reads:

$$\frac{R_{ct}^{ss}}{R_{tdn}^{ss}} = \frac{\varepsilon_n}{k_s} \tag{6.13}$$

438 Monitoring the charge transfer and trapping/detrapping resistances by IS is
439 therefore very useful for the optimization of the onset photovoltage of the
440 photoanodic reaction and the maximum achievable photoanodic current.

441 Finally, the simple Randles circuit (Fig. 6.13c) has been also employed to model
442 the carrier dynamics of Fe_2O_3 photoanodes in the dark and under illumination when
443 a hole scavenger is present in the solution, since only one arc was present in the
444 measured Nyquist plots, and there was no evidence of the presence of the surface
445 state affecting the carrier dynamics of the system. Note, however, that in this case
446 the extracted charge transfer resistance from the valence band is the series combi-
447 nation of the recombination and charge transfer resistances of Fig. 6.13a.
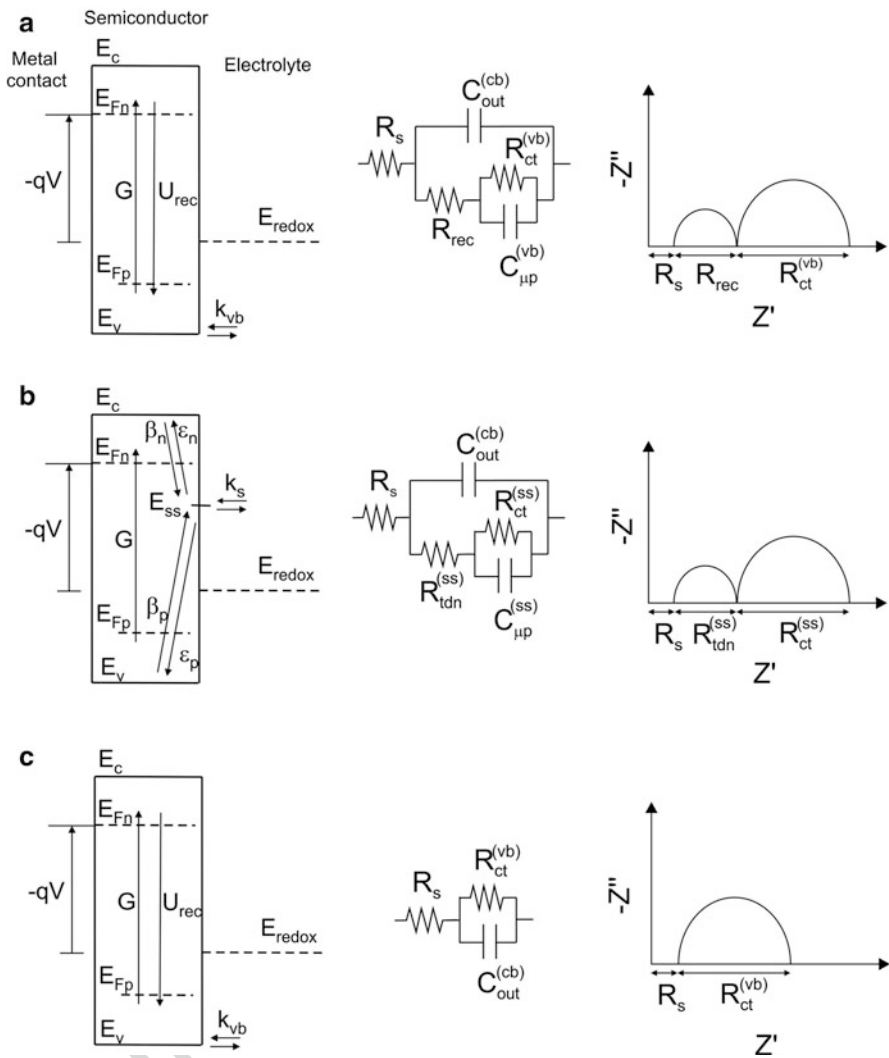
Fig. 6.13 Main simplifications of the kinetic model of Fig. 6.9 available in the literature for the interpretation of experimental data, the associated equivalent circuit (EC) obtained from a small ac perturbation, and the corresponding complex plane IS spectra for (**a**) the direct hole transfer model, (**b**) the indirect hole transfer model, and (**c**) the reduced direct charge transfer model. In these circuits, $C_{out}^{(cb)}$ is the semiconductor capacitance, $C_{\mu p}^{(ss)}$ is the surface state chemical capacitance, R_{rec} is the band to band recombination resistance, $R_{ct}^{(vb)}$ is the hole transfer resistance from the valence band, $R_{tdn}^{(ss)}$ is the trapping/detrapping resistance of electrons from the conduction band, and $R_{ct}^{(ss)}$ is the hole transfer resistance from the surface states. Note that in the case (**c**), the total charge transfer resistance is the serial combination of both resistances involved in case (**a**) (R_{rec} and $R_{ct}^{(vb)}$)

6.5.3 Types of Analysis of IS Results

It should be pointed out that in the literature, two main approaches are considered for the interpretation of IS spectra. One relies on the full numerical resolution of transport and charge transfer equations. The other one consists in proposing a simplified analytical treatment of the impedance, which can be interpreted in terms of EC. The advantage of the first approach is that it allows taking into account more features and is certainly more accurate than the analytical approach. However, as any experimental technique, IS interpretation is limited by the amount of information one can extract from the experimental data. The equivalent circuit is therefore an excellent tool to discriminate between the main dominant features that can be experimentally unveiled. For instance, the model of Fig. 6.9b presents a high number of features and experimental data impose a reduction of this circuit in order to treat the available data, as suggested in Fig. 6.13.

Nonetheless, the EC approach presents two main issues. Firstly, we should recall that IS is a *two contact measurement* so that the information of different internal loci in the sample may be lumped into a single EC element. Secondly, the expression of a given impedance model may be interpreted in terms of several equivalent circuit representations. In order to tackle both issues, it is therefore necessary to perform further experiments and verify the physical meaning of the extracted parameters. One possibility consists in plotting the voltage variations of the capacitances and resistances obtained with a given EC.

In view of these considerations, let us further comment on the EC models discussed above. The ECs presented in Fig. 6.13a, b are identical but the electrical components of those circuits differ by their physical nature. In particular, the low frequency capacitances are of high interest and give valuable information on the origin (surface states or valence band) of the photogenerated holes involved in the water photo-oxidation. The distinction between both types of low frequency capacitances can be operated via a voltage dependence study. In fact, the valence band chemical capacitance follows the variations of the hole population in the valence band and reaches saturation at anodic voltages, as suggested in Fig. 6.14 (*blue line*). On the contrary, surface states, filled with electrons at cathodic applied bias, are progressively filled with holes when applying anodic bias. This transition of the surface state occupation leads to a peak behavior of the surface state capacitance with voltage as shown in Fig. 6.14 (*red line*). Therefore, low frequency capacitance measurements appear to be a valuable tool in order to identify the origin of the photogenerated carriers involved in solar fuel production.

6.5.4 Experimental Results

Recent studies on the photo-oxidation of water with Fe_2O_3 have clearly shown the presence of surface states, which are intrinsic to the semiconductor–water interface and determine the photocurrent onset, approximately 0.5 V more positive
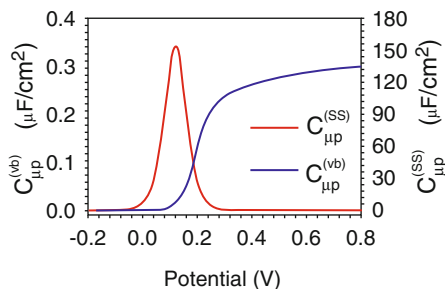
Fig. 6.14 Low frequency capacitances for the direct charge transfer model of Fig. 6.11a (1) and the indirect charge transfer model of Fig. 6.11a (2). The former one is associated to hole storage in the valence band while the latter one is related to hole accumulation in surface states. The steady-state electrical magnitudes and parameters involved in the calculations of these capacitances are the ones obtained from the full drift-diffusion simulations of Fig. 6.11. Reproduced with permission from Bertoluzzi et al. (2016)

than the flat band potential (Klahr et al. 2012a, b, c). Indeed, when an efficient hole scavenger is present in the electrolyte, these surface states are not detectable by impedance spectroscopy and the onset of the photocurrent is cathodically shifted to the flat band potential. Figure 6.5 illustrates this situation showing in panel (a) the jV curves for a Fe_2O_3 photoanode under illumination in contact with an aqueous solution (pH 6.9) and with a $[Fe(CN)_6]^{3-/4-}$ redox couple. Panel (b) shows the total resistance obtained from impedance spectroscopy (symbols) and by derivation of the jV curve (lines), consistently indicating that charge transfer to the solution is more favorable in the presence of the hole scavenger at applied bias below 1.3 V vs. RHE. The characteristic complex plane impedance plots obtained for both systems under illumination at two different applied biases are shown in Fig. 6.6. At lower bias (1.3 V vs. RHE, Fig. 6.6a), the development of one or two arcs is related to the presence or absence of the hole scavenger in the solution, respectively. The high frequency arc in water photo-oxidation is related to the space charge capacitance in the semiconductor material and the low frequency arc conveys information of the capacitance of the surface state. At higher applied bias (1.6 V vs. RHE, Fig. 6.6b), the impedance spectra for water oxidation is reduced to one single semicircle associated to the space charge capacitance, as explained in Sect. 6.5.2.

Fitting the experimental data of Fig. 6.6 to the circuit depicted in Fig. 6.13b, a surface state capacitance, $C_{\mu p}^{ss}$, can be extracted, which follows a characteristic Gaussian-like dependence with applied voltage. The maximum of this capacitance is located close to the photocurrent onset suggesting that accumulation of holes at the surface state is needed before a steady-state photocurrent for water oxidation can be sustained (Fig. 6.15). On the other hand, the minimum of charge transfer resistance coincides with the inflection point of the jV curve. The density of states obtained by Eq. (6.11) can be mapped as shown in Fig. 6.16 for two different pH conditions and exhibits a maximum at approximately 1.23 V vs. RHE, suggesting that multistep water oxidation intermediates are strongly connected to these surface states.
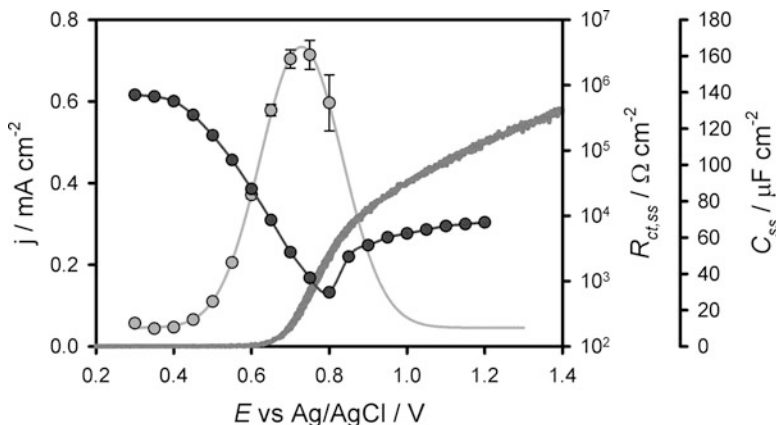
Fig. 6.15 *jV* curve (*dark gray solid line*), C_{ss} (*gray circles*) and $R_{ct,ss}$ (*black circles*) values obtained for a 60 nm hematite electrode under 1 sun illumination and pH 6.9. Adapted with permission from Klahr et al. (2012c)

Fig. 6.16 DOS as a function of RHE reference potential for pH 6.9 (*black circles* and *line*) and pH 13.2 (*triangles* and *gray lines*) under 1 sun illumination. Reproduced with permission from Klahr et al. (2012c)
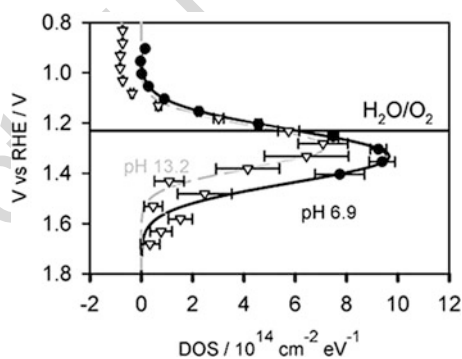
518 An important feature of the surface state capacitance measured by IS and other
519 complementary techniques such as cyclic voltammetry is that it is strongly depen-
520 dent on the nature of the semiconductor/electrolyte interface and the deposition
521 technique. For instance, the distribution of hematite surface states changes drasti-
522 cally in presence of water, methanol, or acetonitrile (Klahr et al. 2015). In addition,
523 the capacitive peak associated to these states shifts anodically with pH (Iandolo and
524 Hellman 2014). In this latter reference, it was demonstrated by DFT that the
525 capacitive response of surface states originates from two types of surface states
526 which differ by their terminations: –O and –OH. The former type of states is close
527 to the middle of the gap and induces recombination while the latter ones are close to
528 the valence band and give rise to hole transfer at higher bias. The formation
529 mechanism of these –O termination was recently proposed by means of DFT + U
530 calculations (Yatom et al. 2015). In particular, they showed that this midgap state
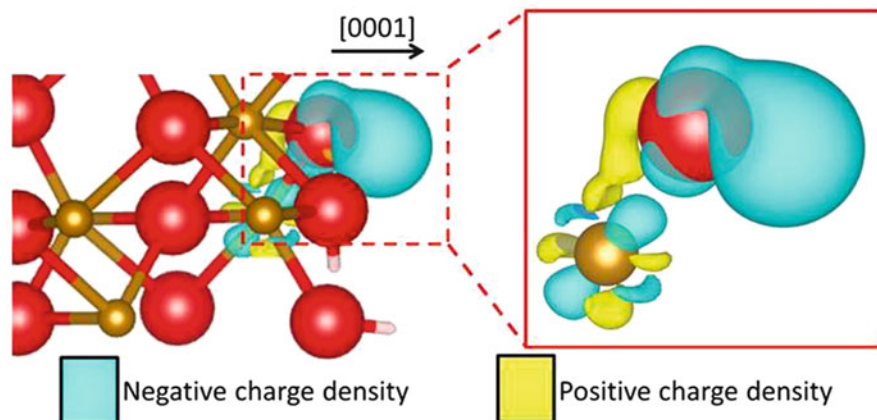
Fig. 6.17 Charge density difference showing a surface state on pure $Fe_2O_3(0001)$. Calculated by subtracting the electron density of the *OH intermediate from the *O intermediate at the fixed ionic positions of the latter. *Red*, *gold,* and *white spheres* denote O, Fe, and H atoms, respectively. Negative and positive charge density iso-surfaces ($\pm 0.01[e/Bohr^3]$) are in *blue* and *yellow*, respectively, where negative being absence of electrons. Reproduced with permission from Yatom et al. (2015)

finds its origin in the hybridization of the d and p orbitals of Fe and O, respectively, as depicted by Fig. 6.17. Concomitantly, Klahr and Hamann (2014) demonstrated the existence of both types of states by impedance spectroscopy and cyclic voltammetry for hematite in aqueous electrolyte. However, the same group showed that the existence of both capacitive features is strongly dependent on the deposition method. In particular, they demonstrated that using atomic layer deposition (ALD) and annealing hematite at 800 °C allows removing recombination centers (Zandi and Hamann 2014). This work echoed an earlier study by Chou et al. (2013) who observed, via low frequency capacitance measurements, that preparation of α-Fe_2O_3 electrodes by Fe oxidation is more favorable to surface state-assisted charge transfer than by anodic electrodeposition.

Similarly, Doyle and Lyons (2013) revealed through IS measurements that hydrous iron oxide is featured by a clear surface state capacitive peak associated to Fe=O intermediates at high pH (concentration of NaOH superior to 1 mol/L). Instead, for lower pH, the measured capacitance was found to be similar to the valence band capacitance displayed in Fig. 6.14 (plot 1). In this case, the EC of Fig. 6.13a must be employed for the fitting of IS data. By comparing surface state capacitance and X-ray spectroscopies of hematite samples under different plasma treatments, Braun and coworkers (Hu et al. 2016) show that iron surface states induce higher reactivity toward water oxidation than oxygen surface states.

The model of charge transfer through surface states has also been successfully employed to explain the photo-oxidation of water on other n-type semiconductor materials such as $CuWO_4$ (Pyper et al. 2013) and TiO_2 nanotubes (Cachet and Sutter 2015). In contrast with the behavior of Fe_2O_3, the presence of Fermi level

555 pinning in the dark suggests that these midgap states are permanent and not
556 photogenerated. Similar approach has been followed to understand carrier dynam-
557 ics on FeS_2 (Caban-Acevedo et al. 2014).

6.6   Band Edge Movement

559 The modification of surface dipoles at the semiconductor–liquid interface origi-
560 nated by different factors leads to a shift of the semiconductor band edges with
561 respect to the stable electrolyte energy level such as the Fermi energy of the redox
562 couple (redox potential). This effect, termed *band edge movement*, or more simply
563 *band shift*, can be monitored by IS. When a space charge region is developed in the
564 semiconductor material in contact with the solution, the change of the flat band
565 potential (V_{fb}) is a clear evidence of band shift. From Eq. (2.29), we recall that the
566 Mott–Schottky plot (if it is reasonably straight) reveals the flat band potential and
567 the doping density of a planar semiconductor electrode. Therefore, electrodes in
568 which the surface conditions have produced a change of the flat band potential
569 must show the Mott–Schottky signature horizontally displaced, and no other
570 changes, since the doping level is obtained by the edge of the space charged
571 region that is inside the semiconductor layer.
572   As an example, Fig. 6.18a shows the *jV* curves of Fe_2O_3 photoanodes under
573 illumination at 100 mW/cm^2 in aqueous electrolyte, a mixture of water and
574 methanol and pure methanol. There exists a clear anodic shift of the photocurrent
575 when pure methanol is employed, which can be at least partially explained by the
576 anodic band shift illustrated in Fig. 6.18b by the change in flat band potential.
577 The origin of this shift is related to the difference in surface dipoles formed at the
578 semiconductor/solution interface. On the other hand, the slopes of the Mott–
579 Schottky plots shown in Fig. 6.18b are practically identical indicating that the
580 donor density is not altered. The extracted doping density, N_D, was calculated to
581 be 5.3×10^{18} cm^{-3}, in good agreement with values previously reported (Klahr
582 et al. 2012a, b, c). In order to account for the band shift, it is more informative to
583 plot the *jV* curves, correcting the applied voltage to the flat band potential, V vs. V_{fb},
584 as shown in Fig. 6.18c. The modulation of flat band potential can also be achieved
585 with thin ferroelectric layer in the semiconductor surface (Yang et al. 2015).
586   As mentioned above, charge localization in surface states also leads to consid-
587 erable changes in the Helmholtz potential that result from trapping. These changes
588 in the potential distribution lead to Fermi level pinning, or band unpinning, as
589 discussed in Sect. 1.2.8. Under illumination, the trapping of minority carriers at
590 surface states produces charging of surface states and the Helmholtz layer, and
591 hence band unpinning as first described by Kelly and Memming (1982). In
592 Fig. 6.19, we show the mechanism of changes of Mott–Schottky plot that are
593 observed when the semiconductor surface undergoes trapping of minority
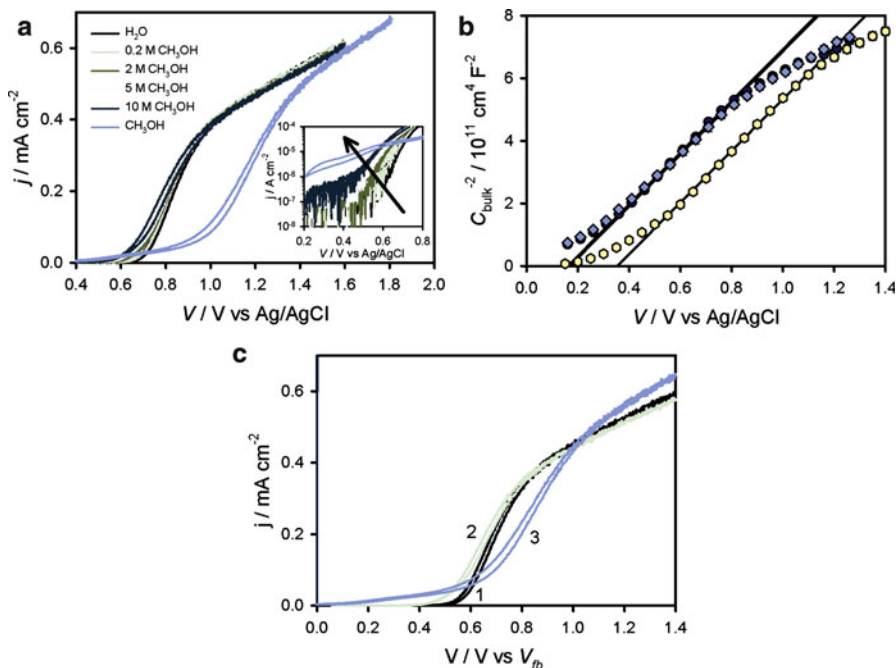
Fig. 6.18 (**a**) jV curve of a hematite electrode in contact with a H_2O and methanol electrolyte under 1 sun illumination. (**b**) Mott–Schottky plot of C_{bulk} measured in the dark for H_2O (*circles*), 5 M CH_3OH (*diamonds*) and CH_3OH electrolytes (*hexagons*). (**c**) jV curves of a hematite electrode under 1 sun illumination in contact with H_2O (*1*), 5 M CH_3OH (*2*) and CH_3OH (*3*) plotted vs. V_{fb}. Adapted with permission from Klahr et al. (2015)

photogenerated carriers. Considering water oxidation with Fe_2O_3, Fig. 6.20 clearly illustrates Fermi level pinning associated to the presence of light-activated surface states. The Mott–Schottky plot of the space charge capacitance under illumination levels off at potentials where the surface state capacitance is measured.

## 6.7 Modification of Charge Transfer Rate

In the context of PEC solar fuels production, the characterization of the charge transfer rate is particularly relevant to monitor the effect of surface modifications of photoelectrodes, for example the deposition of co-catalysts (Klahr et al. 2012b; Badia-Bou et al. 2013; Riha et al. 2013), passivation layers (Le Formal et al. 2011; Steier et al. 2014), and the formation of homo or heterojunctions at the surface to displace energy levels (Li et al. 2012; Lin et al. 2012). IS is a widely used tool to assess changes in the photoelectrode charge transfer rate after the above-mentioned treatments. Nevertheless, many times the impedance study is exclusively based on the comparison of the complex impedance plots obtained from different samples at
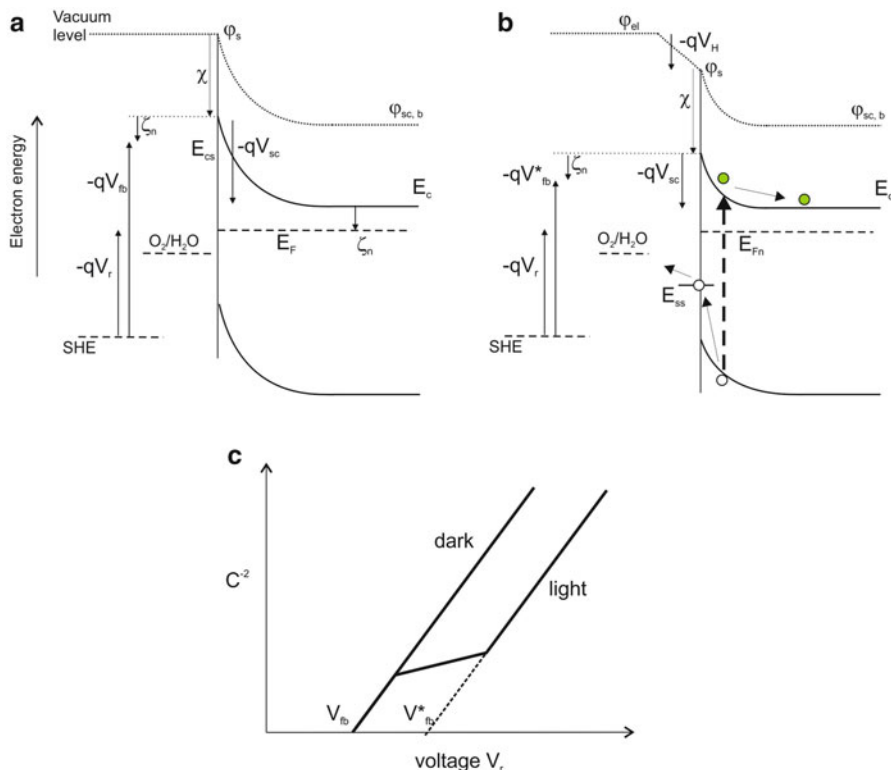
Fig. 6.19 Energy diagram of a semiconductor/electrolyte junction, in which the semiconductor has a surface state that captures both minority and majority carriers, and transfers carriers to the electrolyte. Under dark (**a**), the surface states cannot be populated with holes and there is no Fermi level pinning effect. Under illumination (**b**), the surface states cannot be populated with holes and there is no Fermi level pinning effect. The Mott–Schottky plot with different regions of capacitance is shown in (**c**). At voltage close to flat band, dark and light curves overlap because the recombination does not allow maintaining holes in the ss. The maximum shift of the flat band potential under illumination is related to the density of surface states and the value of the Helmholtz capacitance

608 a single applied bias, and the reported information does not go further than an R_{dc}
609 value which could be obtained faster by dc methods. In order to fully exploit the
610 power of this technique, the evolution of the EC components extracted from fitting
611 the IS response with applied potential must be examined. The information provided
612 by the charge transfer resistances coupled to that of the capacitances provides
613 valuable insights on the basic mechanisms responsible for the functional enhance-
614 ment observed.

615   Figure 6.21 shows the jV curves together with values of film capacitance and
616 charge transfer resistance for a Fe_2O_3 photoelectrode coated with Co–Pi layers by
617 photo-assisted electrodeposition with different thickness values (controlled by the
618 charge passed through the electrodes). The capacitance of the films (Fig. 6.21a)
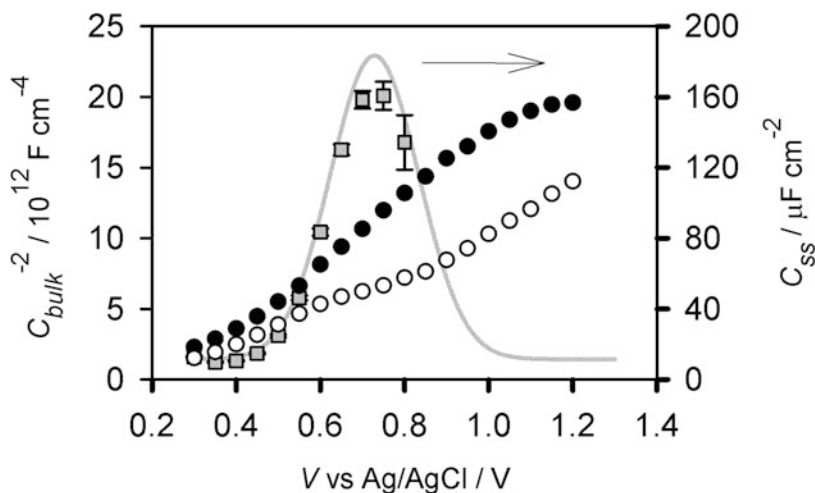
Fig. 6.20 Mott–Schottky plots at pH 6.9 in the dark (*black circles*) and under 1 sun (*open circles*). A plot of the trap state capacitance, C_{ss}, (*gray squares*) is superimposed to show the Fermi level pinning. Reproduced with permission from Klahr et al. (2012c)

increases with the Co–Pi thickness, indicating that the "catalyst" controls the capacitive behavior of the electrodes. This increase of capacitance is correlated to a concomitant decrease of the charge transfer resistance (Fig. 6.21b), responsible for the faster water oxidation kinetics, which leads to the improved performance displayed in the *jV* curves (Fig. 6.21c) upon Co–Pi addition (Klahr et al. 2012b), see also Fig. 6.4. According to this picture, the Co–Pi catalyst can be seen as an efficient hole collector, which stores the photogenerated holes from the hematite electrode. This charge separation reduces recombination at the surface of Fe_2O_3, which results in lower photocurrent onset potentials and hence improved water oxidation efficiency. A similar mechanism has been demonstrated for IrO_x catalyst on Fe_2O_3 (Badia-Bou et al. 2013). The evolution of film capacitance, charge transfer resistance, and photocurrent with applied voltage follows the same behavior observed for Co–Pi, validating the same interpretation provided for this catalyst. Upon deposition of either Co–Pi or IrO_x on Fe_2O_3, any effects related to band shift were discarded, as derived from Mott–Schottky plots of the space charge capacitance. Cobalt-based materials have also been studied as catalysts for hydrogen evolution reaction. Recently, a heterostructure composed of p-Si microwires decorated with $CoSe_2$ nanorods was proposed as a promising noble metal-free photocathode candidate for solar fuel production (Basu et al. 2015). A typical volcano plot was recorded between the obtained photocurrent and the catalyst loading, which was thoroughly analyzed by optical and IS measurements. From optical absorption, it was ruled out an effect of light inhibition as responsible for the drop in photocurrent of the $CoSe_2$-richest sample. Impedance complex plane plots resolved a separated contribution of each interface of the heterostructure, i.e. $Si/CoSe_2$ and $CoSe_2$/electrolyte. From the study of the extracted resistances, it was predicted that an increased $CoSe_2$ loading on

Fig. 6.21 (**a**) Capacitance of Fe_2O_3/Co–Pi films ($C_{Co–Pi}$) and (**b**) Charge transfer resistance ($R_{ct,Co–Pi}$) fitted from impedance response of hematite electrodes with 1 (*triangles pointing down*), 2 (*squares*), 15 (*diamonds*), 45 (*triangles pointing up*), and 90 mC/cm^2 (*hexagons*) Co–Pi deposited. Bare hematite fitting parameters of (**a**) C_{ss}, (**b**) $R_{ct,ss}$ are shown for comparison (*red open circles*). (**c**) Corresponding jV curves obtained by cyclic voltammetry. Reproduced with permission from Klahr et al. (2012b)
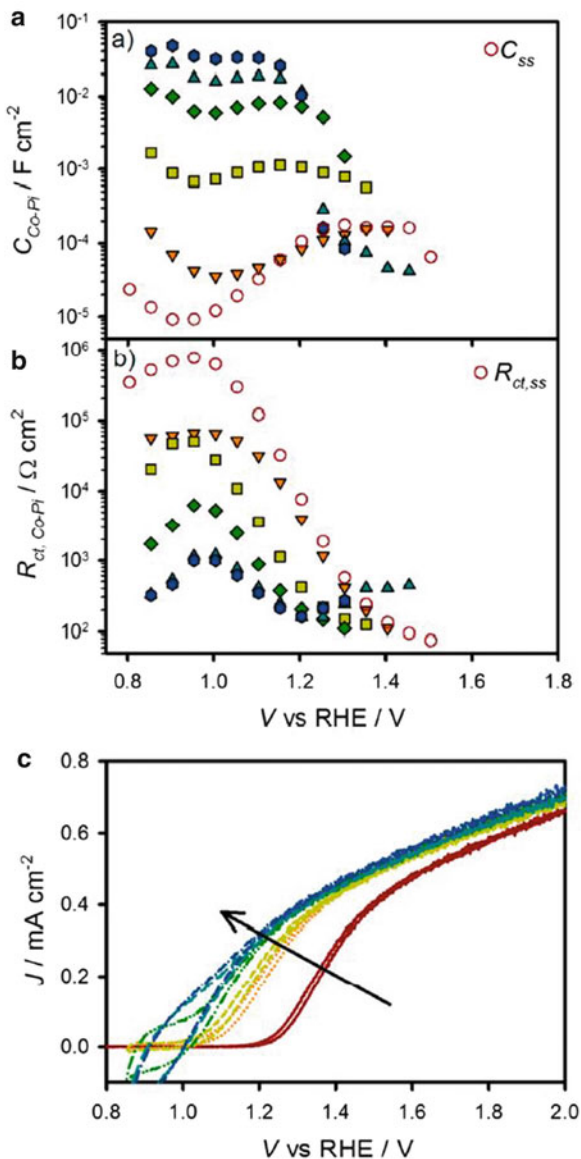
644 the microwired semiconductor acts as charge recombination centres which restricts
645 the charge transfer, playing against the reported catalytic effect of the semimetallic
646 nanorods.
647   On the other hand, the deposition of Ga_2O_3 overlayers on Fe_2O_3 photoelectrodes,
648 Fig. 6.22, also yields a favorable cathodic shift of the photocurrent onset, which is
649 associated to the passivation of surface states at the Fe_2O_3 interface (Steier

et al. 2014). This surface passivation has been identified by the decrease of the peak capacitance associated to the density of surface states. Additionally, a cathodic shift of the density of surface states was observed, probably indicating a change in the water oxidation mechanism. It is interesting to note that Ga_2O_3 does not exhibit any electrocatalytic behavior when deposited on top of FTO substrates, and does not induce any band shift when deposited on top of Fe_2O_3. This idea of surface state passivation of Ga_2O_3 coated Fe_2O_3 electrodes seems to be valid for the 13-group oxide overlayers with the corundum structure, which have been reported to release lattice strain of ultrathin hematite layers and decrease the density of surface states (Hisatomi et al. 2011). Photoluminescence experiments carried out on Fe_2O_3/Al_2O_3 systems corroborate this idea of surface states passivation, as showed in Fig. 6.23 (Le Formal et al. 2011). Another study has provided integral characterization of the passivation of Ti-doped hematite (Monllor-Satoca et al. 2015).

Studies with $WO_3/BiVO_4$ heterostructures have also shown that the charge transfer resistance is directly related to the catalytic behavior as well as the functional performance of the electrodes (Hong et al. 2011). Recently, Shi et al. (2015) thoroughly demonstrated by a systematic optoelectronic and photoelectrochemical study that the improved performance in the heterojunction was connected to a synergism between the adequate optical properties of $BiVO_4$ and the excellent charge transfer properties of WO_3, which controls both the transport and capacitive response in the composite.

6.8 Transport and Reaction in Nanostructures

In nanostructured semiconductor materials, charge transport and charge transfer (or reaction) are often coupled and impedance spectroscopy allows deconvolution of these phenomena by the use of complex physical models, generally including a transmission line element. A classical example is found in nanostructured TiO_2 films, which are the base of photoelectrochemical solar cells like (dye or quantum dot) sensitized solar cells (Wang et al. 2006; Raga et al. 2012). When these nanostructures are integrated as photoelectrodes for solar fuels production, impedance spectroscopy provides a powerful tool for the analysis of charge transport, charge transfer, and charge accumulation mechanisms, which are key factors to evaluate the functional performance of the device. Figure 6.24a represents the general transmission line equivalent circuit. This representation takes into account electron transport (r_{tr}), along the electron transport level. The transversal element ζ_m in Fig. 6.24a depends on charge accumulation and charge transfer, and the lower, resistanceless rail indicates fast transport in the electrolyte. Now considering the process of water oxidation, we take into account the presence of both electrons and holes in the semiconductor material, which is a situation absent in a sensitized solar cell. In this case, a more complex model is needed, and we suggested the circuit of Fig. 6.9b, which has been previously developed for the presence of electrons and holes in related systems. This equivalent circuit, that constitutes the
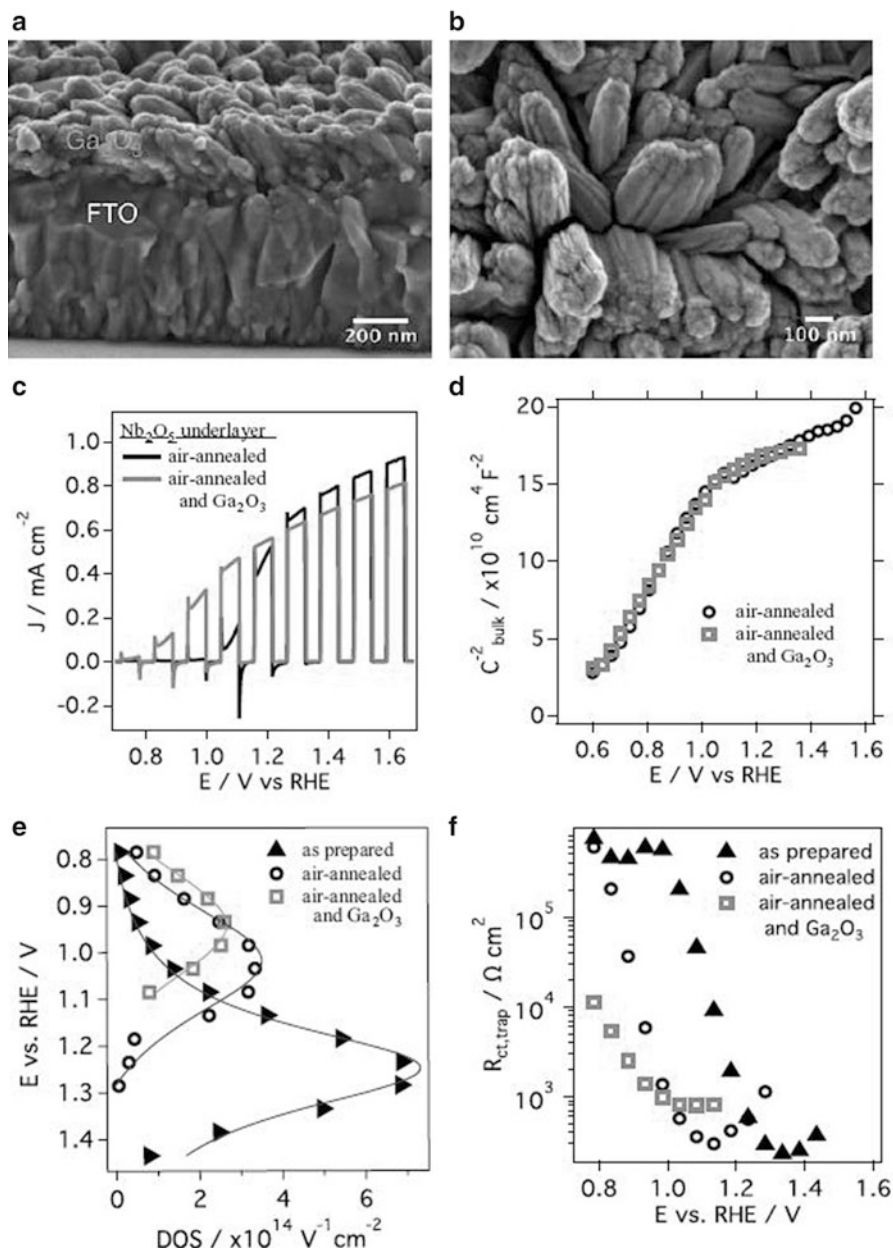
Fig. 6.22 Characteristics of hematite photoanodes upon addition of a Ga_2O_3 overlayer on a Nb-doped hematite photoanode. Shown are (**a**) cross-sectional and (**b**) top-view SEM images of the Ga_2O_3 structure on a (barely visible) ultrathin (approximately 16 nm) hematite layer deposited on FTO glass. (**c**) Light chopping experiments of air-annealed Nb-doped thin (approximately 30 nm) hematite photoanodes before (*black*) and after Ga_2O_3 CBD (*gray*). (**d**) Mott–Schottky plots of the samples shown in (**c**) measured in the dark. (**e**) Applied potential versus density of surface states (DOS) extracted from C_{ss}. Shown are air-annealed samples from (**c**) before (*black hollow circles*) and after Ga_2O_3 deposition (*gray hollow squares*). In addition, a nonannealed sample is
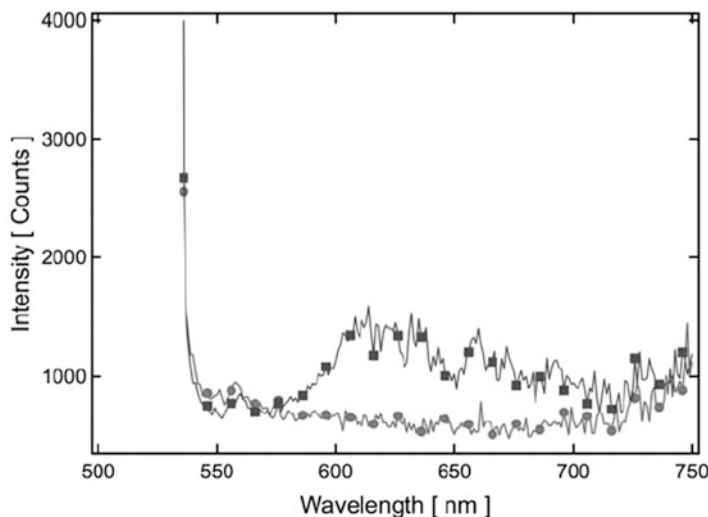
Fig. 6.23 Photoluminescence emission spectra (excitation wavelength 520 nm) of a hematite cauliflower-type nanostructure photoanode before (*circles*) and after three ALD cycles of Al_2O_3 on its surface (*squares*). Reproduced with permission from Le Formal et al. (2011)

element ζ_m in Fig. 6.24a, is composed of separate chemical capacitances of 691 electrons and holes ($C_{\mu p}^{(cb)}$ and $C_{\mu p}^{(vb)}$) and charge transfer to the solution through 692 the conduction and valence bands ($r_{ct}^{(cb)}$ and $r_{ct}^{(vb)}$) together with electron and hole 693 trapping ($r_{trn}^{(ss)}$ and $r_{trp}^{(ss)}$) and charge transfer through the surface state ($r_{ct}^{(ss)}$). A 694 simplified equivalent circuit only accounting for the transport, chemical capaci- 695 tance, and charge transfer of electrons from the conduction band is represented in 696 Fig. 6.24b. If the system shows easy hole transport in the valence band, the model 697 should be extended with a channel for hole transport, included in the equivalent 698 circuit, as indicated in Fig. 6.24c. In this situation, the model shows the upper rail 699 for electron transport, the lower one for hole transport, and the central one for the 700 electrolyte. In Fig. 6.24c, the rectangular box does not represent an impedance 701 element but indicates a more complex connection, depending on the specific charge 702 storage, recombination, surface states features, and other specific properties that 703 link electrons, holes, and their charge transfer to the solution. There are some 704 illustrative examples in the literature describing the carrier dynamics of nanostruc- 705 tured photoanodes of several metal oxides by these advanced models, particularly 706

◄

Fig. 6.22 (continued) shown for comparison (*black filled triangles*). A Lorentzian fit for each sample guides the eye but also indicates the shift in maximum of the DOS at a certain potential. (**f**) Charge transfer resistances from surface states, $R_{ct,trap}$, versus applied potential for samples from (**e**) show a minimized resistance in presence of a Ga_2O_3 overlayer. Measurements shown in (**c**), (**e**), and (**f**) were carried out with simulated AM 1.5G (100 mW/cm^2) light. The electrolyte was 1 M NaOH (pH 13.6). Adapted with permission from Steier et al. (2014)
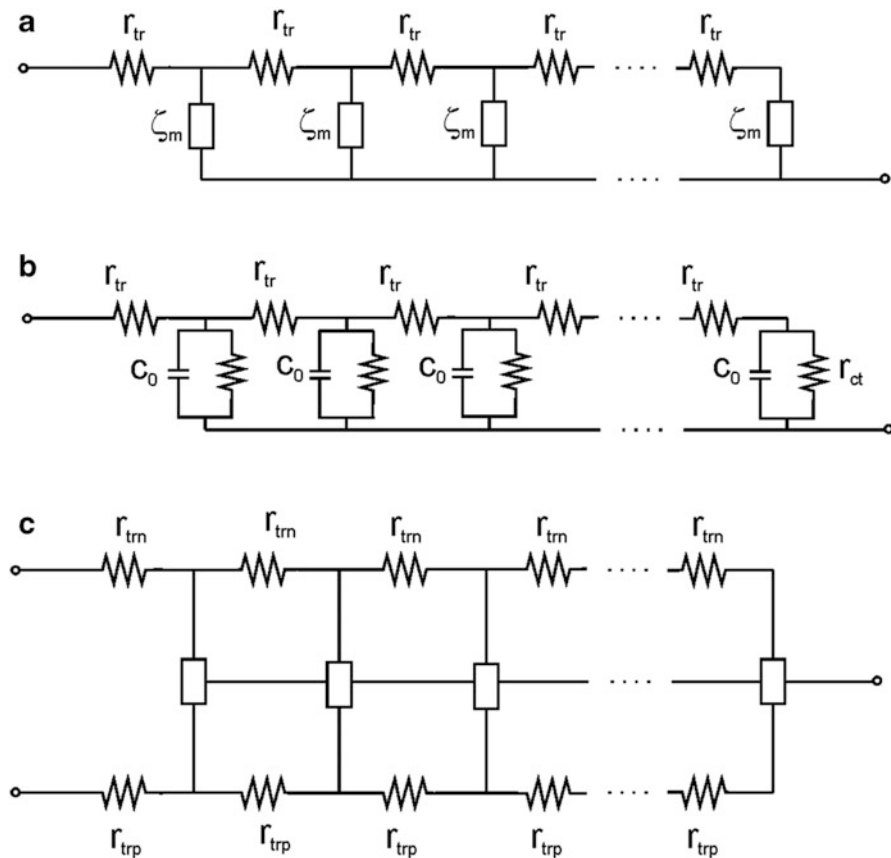
Fig. 6.24 (**a**) Two channel transmission line equivalent circuit, with electron transport resistance and the transversal element ζ_m corresponds to the equivalent circuit represented in Fig. 6.10b. (**b**) Simplified equivalent circuit used in the present study including transport, chemical capacitance, and charge transfer of electrons. (**c**) Equivalent circuit including electron and hole transport and the central electrolyte rail. The *box* does not represent an impedance element but indicates a more complex connection, depending on the kinetic processes of electrons and holes

707 by the model showed as Fig. 6.24b: TiO_2 (Fabregat-Santiago et al. 2005; Gimenez
708 et al. 2012; Rodenas et al. 2013; Trevisan et al. 2013), ZnO (Martinson et al. 2009)
709 WO_3 (Balandeh et al. 2015) and Fe_2O_3 (Cummings et al. 2012).

## 710 6.8.1   Transport and Charge Transfer

711 In order to present a representative example of application of the transmission line
712 model established in Fig. 6.24b, Fig. 6.25a shows the complex plane impedance
713 plots for films of TiO_2 nanoparticles with different thickness. The marked area in
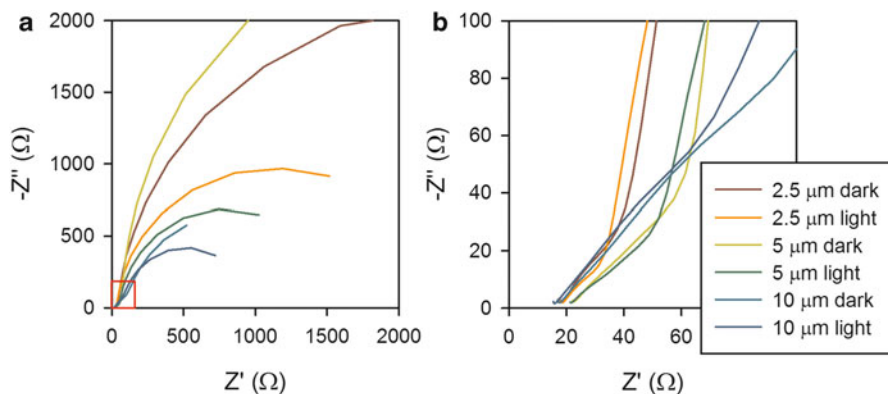
Fig. 6.25 (**a**) EIS spectra obtained for nanoparticulated films of TiO_2 at -0.95 V vs. Ag/AgCl in the dark and under illumination at 100 mW/cm^2. (**b**) Magnification of the *squared area* in (**a**) to illustrate the 45° line related to transport resistance

Fig. 6.25a is showed as Fig. 6.25b. In this figure, the high frequency region clearly   714
shows the 45° line characteristic of electron diffusion. It is clear that the length of   715
this line increases with film thickness, evidencing that transport limitations are   716
more important in thick films. From the model fitting, the chemical capacitance for   717
electrons, C_μ, the charge transfer resistance, R_{ct}, and the resistivity (ρ_{TiO2}) of the   718
TiO_2 architectures could be extracted. As previously mentioned, C_μ monitors the   719
electronic density of states at the Fermi level and probes the distribution of trap   720
states below the conduction band. ρ_{TiO2} is the reciprocal conductivity and R_{ct} is   721
related to the transfer of electrons at the TiO_2/solution interface (Bisquert 2002;   722
Bisquert et al. 2004). These three quantities describe the main electronic mecha-   723
nisms for the operation of the device. Figure 6.26 shows an example of the obtained   724
results for the fitting of films of TiO_2 hollow nanowires (HNWs) and nanoparticles   725
(NPs) sensitized with CdSe quantum dots by two different methods (Chemical Bath   726
Deposition, CBD and Successive Ionic Layer Adsorption and Reaction, SILAR):   727
the chemical capacitance exhibits the expected exponential dependence with poten-   728
tial, reflecting the exponential tail of the density of states of TiO_2 below the   729
conduction band. To compare both transport and charge transfer resistances   730
between the different specimens with the same density of electrons, the chemical   731
capacitances of all samples were shifted to make them overlap and the corrected   732
potential is termed "equivalent conduction band potential" (V_{ecb}). In spite of the   733
one-dimensional nature of the hollow nanowires, the resistivity exhibits very   734
similar values compared to nanoparticles. This could be explained by the polycrys-   735
talline nature of the nanowires since grain boundaries are preferential sites for   736
recombination and can slow down charge transport through the material, decreasing   737
the wire conductivity.   738

Fig. 6.26 Parameters extracted after fitting the impedance spectroscopy spectra of TiO₂ nanoparticles (NPs) and hollow nanowires (HNWs) and NPs sensitized by different methods, chemical bath deposition (CBD) and successive ionic layer adsorption and reaction (SILAR), using the model presented in Fig. 9.22c. (**a**) Chemical capacitance (C_μ), (**b**) TiO₂ resistivity (ρ_{TiO2}) and (**c**) recombination resistance (R_{ct}) as a function of potential (**a**), and versus the equivalent conduction band potential (V_{ecb}) (**b** and **c**). All impedance measurements were carried out in the dark. The lines in (**b**) are linear fittings of the experimental data. In (**c**) lines are drawn as eye guides. Reproduced with permission from Rodenas et al. (2013)
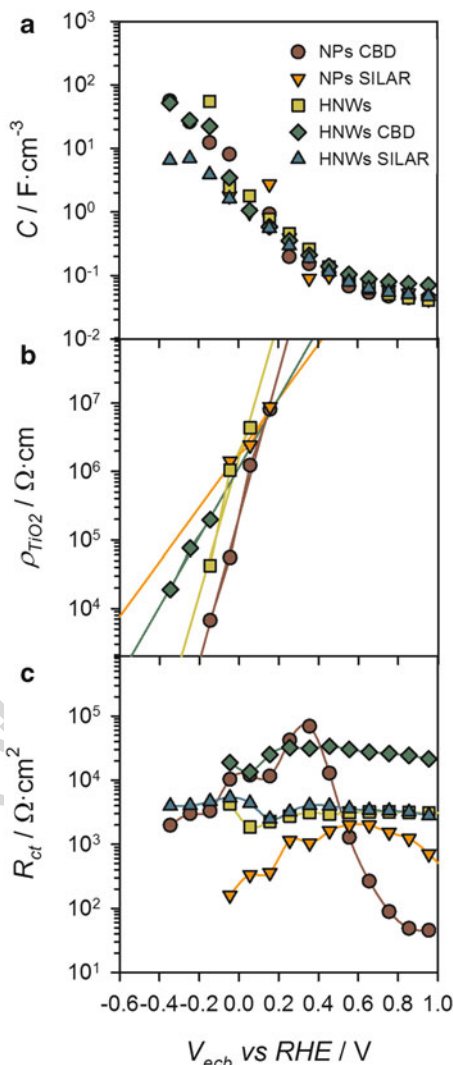
6.8.2 Determination of Band Edge Shift by Displacement of the Chemical Capacitance

When we consider a nanostructured semiconductor electrode, if the characteristic dimension is lower than the Debye length, the bands of the material cannot bend at the surface due to the small available size. The band edge displacement by surface modification appears as an overall displacement of the electronic energy levels of the semiconductor that can be monitored by the measurement of the chemical capacitance (C_μ) that provides a powerful tool to understand band shift effects.

There are several examples in the literature for TiO_2 nanostructured electrodes in the field of photovoltaic and photoelectrochemical devices, as described in the previous section. A recent illustrative example shows that the deposition of carbon nitride (C_3N_4) on nanostructured TiO_2 scaffolds leads to the development of a large surface dipole (Xu et al. 2015). The TiO_2/C_3N_4 hybrid films were prepared by an in situ vapor-transport growth mode, using cyanuric acid–melamine (CM) or cyanuric acid–melamine–barbituric acid (CMB) supramolecular complexes as the precursor (labeled here as TiO_2/CM and TiO_2/CMB, respectively). Figure 6.27a shows the cyclic voltammetry curves obtained in 0.1 M Na_2S solution for C_3N_4-modified TiO_2 substrates and comparison with reference TiO_2 electrodes. The voltammograms reflect the capacitive effects associated to the increasing density of states in the cathodic bias direction, typically reported on TiO_2 films (Bisquert 2014). Furthermore, it is also identified a cathodic peak at -0.6 V vs. Ag/AgCl for bare TiO_2, which is related to electron transfer through a localized bandgap state in TiO_2. For both C_3N_4-modified TiO_2 substrates, this peak is clearly shifted to more positive potentials. In order to confirm that this movement is related to band shift, IS measurements were carried out. The obtained complex plane impedance plots were fitted by using the transmission line model described in Fig. 6.24b, accounting for the coupling of transport and recombination with the electrolyte (Bisquert 2002; Wang et al. 2006). Figure 6.27b shows the evolution of the extracted chemical capacitance for TiO_2, C_μ, with the applied reference electrode potential, and displays the exponential density of states of TiO_2 below the conduction band (Bisquert 2014). The slope of the C_μ versus the potential, in the semilogarithmic scale, is similar for all the electrodes, which indicates that the deposition of C_3N_4 does not significantly modify the DOS of TiO_2. However, a clear anodic shift of about 200 mV is observed for C_μ of the C_3N_4 sensitized TiO_2 electrodes, related to the downward displacement of the TiO_2 conduction band. This is consistent with a strong dipole formation after C_3N_4 deposition.
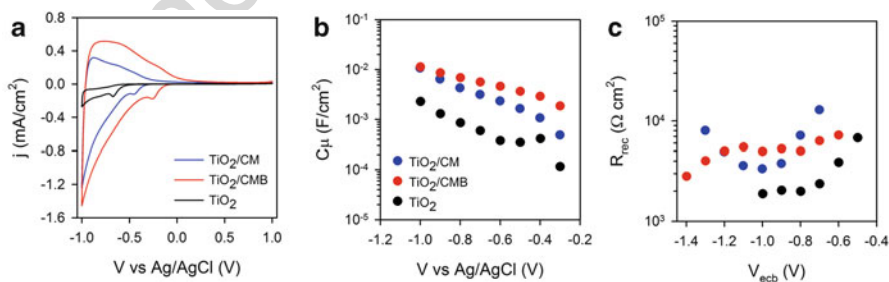
Fig. 6.27 (**a**) Cyclic voltammetry, (**b**) chemical capacitance (C_μ), and (**c**) recombination resistance (R_{rec}) of pristine TiO_2, TiO_2/CM, and TiO_2/CMB substrates obtained in the dark. The measurement was carried out in a three-electrode system, Pt as the counter and Ag/AgCl as the reference electrode and 0.1 M Na_2S solution as the electrolyte. Reproduced with permission from Xu et al. (2015)

6.9 Conclusions

Our analysis of the transport, recombination, and charge transfer processes at the semiconductor/electrolyte system indicates that this is a problem of great complexity due to the combination of different carriers and sequential processes that determine the overall performance. One principal problem is the distinction between direct transfer from the extended states of valence band versus the hole transfer from surface states at an illuminated photoanode. We have described a variety of models that provide criteria for the separation of the different processes according to the interpretation of capacitances in the system. Similarly, IS can provide a great deal of information on the operation of catalyzed surfaces and the identification of band edge shifts. Finally, nanostructured porous electrodes are characterized by significant variation of carrier density and conductivity, and these features can be established using the distributed transmission line models.

References

Allongue P, Cachet H (1984) I-V curve and surface state capacitance at illuminated semiconductor/liquid contacts. J Electroanal Chem 176:369–375

Badia-Bou L, Mas-Marza E, Rodenas P, Barea EM, Fabregat-Santiago F, Gimenez S, Peris E, Bisquert J (2013) Water oxidation at hematite photoelectrodes with an iridium-based catalyst. J Phys Chem C 117:3826–3833

Balandeh M, Mezzetti A, Tacca A, Leonardi S, Marra G, Divitini G, Ducati C, Meda L, Di Fonzo F (2015) Quasi-1D hyperbranched WO_3 nanostructures for low-voltage photoelectrochemical water splitting. J Mater Chem A 3:6110–6117

Basu M, Zhang Z-W, Chen C-J, Chen P-T, Yang K-C, Ma C-G, Lin CC, Hu S-F, Liu R-S (2015) Heterostructure of Si and $CoSe_2$: a promising photocathode based on a non-noble metal catalyst for photoelectrochemical hydrogen evolution. Angew Chem Int Ed 54:6211–6216

Bertoluzzi L, Bisquert J (2012) Equivalent circuit of electrons and holes in thin semiconductor films for photoelectrochemical water splitting applications. J Phys Chem Lett 3:2517–2522

Bertoluzzi L, Lopez-Varo P, Jimenez Tejada JA, Bisquert J (2016) Charge transfer processes at the semiconductor/electrolyte interface for solar fuel production: insight from impedance spectroscopy. J Mater Chem A 4:2873–2879

Bisquert J (2002) Theory of the impedance of electron diffusion and recombination in a thin layer. J Phys Chem B 106:325–333

Bisquert J (2008) Beyond the quasi-static approximation: impedance and capacitance of an exponential distribution of traps. Phys Rev B 77:235203

Bisquert J (2010) Theory of the impedance of charge transfer via surface states in dye-sensitized solar cells. J Electroanal Chem 646:43–51

Bisquert J (2014) Nanostructured energy devices: equilibrium concepts and kinetics. CRC Press, Boca Raton

Bisquert J, Fabregat-Santiago F (2010) In: Kalyanasundaram K (ed) Dye-sensitized solar cells. CRC Press, Boca Raton

Bisquert J, Cahen D, Hodes G, Ruhle S, Zaban A (2004) Physical chemical principles of photovoltaic conversion with nanoparticulate, mesoporous dye-sensitized solar cells. J Phys Chem B 108:8106–8118

Caban-Acevedo M, Kaiser NS, English CR, Liang D, Thompson BJ, Chen H-E, Czech KJ, Wright JC, Hamers RJ, Jin S (2014) Ionization of high-density deep donor defect states explains the low photovoltage of iron pyrite single crystals. J Am Chem Soc 136:17163–17179

Cachet H, Sutter EMM (2015) Kinetics of water oxidation at TiO_2 nanotube arrays at different pH domains investigated by electrochemical and light-modulated impedance spectroscopy. J Phys Chem C 119:25548–25558

Cendula P, Tilley SD, Gimenez S, Bisquert J, Schmid M, Grätzel M, Schumacher JO (2014) Calculation of the energy band diagram of a photoelectrochemical water splitting cell. J Phys Chem C 118:29599–29607

Chou J-C, Lin S-A, Lee C-Y, Gan J-Y (2013) Effect of bulk doping and surface-trapped states on water splitting with hematite photoanodes. J Mater Chem A 1:5908–5914

Cummings CY, Marken F, Peter LM, Wijayantha KGU, Tahir AA (2012) New insights into water splitting at mesoporous alpha-Fe_2O_3 films: a study by modulated transmittance and impedance spectroscopies. J Am Chem Soc 134:1228–1234

Dareedwards MP, Goodenough JB, Hamnett A, Trevellick PR (1983) Electrochemistry and photoelectrochemistry of Iron(III) oxide. J Chem Soc Farad Trans I 79:2027–2041

Doyle RL, Lyons MEG (2013) An electrochemical impedance study of the oxygen evolution reaction at hydrous iron oxide in base. Phys Chem Chem Phys 15:5224–5237

Fabregat-Santiago F, Bisquert J, Garcia-Belmonte G, Boschloo G, Hagfeldt A (2005) Influence of electrolyte in transport and recombination in dye-sensitized solar cells studied by impedance spectroscopy. Sol Energy Mater Sol Cells 87:117–131

Fabregat-Santiago F, Garcia-Belmonte G, Mora-Seró I, Bisquert J (2011) Characterization of nanostructured hybrid and organic solar cells by impedance spectroscopy. Phys Chem Chem Phys 13:9083–9118

Freund T, Morrison SR (1968) Mechanisms of cathodic processes on semiconductor Zinc Oxide. Surf Sci 9:119

Gimenez S, Dunn HK, Rodenas P, Fabregat-Santiago F, Miralles SG, Barea EM, Trevisan R, Guerrero A, Bisquert J (2012) Carrier density and interfacial kinetics of mesoporous TiO_2 in aqueous electrolyte determined by impedance spectroscopy. J Electroanal Chem 668:119–125

Hens Z (1999) The electrochemical impedance on one-equivalent electrode processes at dark semiconductor redox electrodes involving charge transfer through surface states. 1. Theory. J Phys Chem B 103:122–129

Hisatomi T, Le Formal F, Cornuz M, Brillet J, Tetreault N, Sivula K, Graetzel M (2011) Cathodic shift in onset potential of solar oxygen evolution on hematite by 13-group oxide overlayers. Energy Environ Sci 4:2512–2515

Hong SJ, Lee S, Jang JS, Lee JS (2011) Heterojunction $BiVO_4$/WO_3 electrodes for enhanced photoactivity of water oxidation. Energy Environ Sci 4:1781–1787

Hu Y, Boudoire F, Hermann-Geppert I, Bogdanoff P, Tsekouras G, Mun BS, Fortunato G, Graetzel M, Braun A (2016) Molecular origin and electrochemical influence of capacitive surface states on iron oxide photoanodes. J Phys Chem C. doi:10.1021/acs.jpcc.5b08013

Iandolo B, Hellman A (2014) The role of surface states in the oxygen evolution reaction on hematite. Angew Chem Int Ed 53:13404–13408

Kelly JJ, Memming R (1982) The influence of surface recombination and trapping on the cathodic photocurrent at p-type III-V electrodes. J Electrochem Soc 129:730–738

Klahr B, Hamann T (2014) Water oxidation on hematite photoelectrodes: insight into the nature of surface states through in situ spectroelectrochemistry. J Phys Chem C 118:10393–10399

Klahr B, Gimenez S, Fabregat-Santiago F, Bisquert J, Hamann TW (2012a) Electrochemical and photoelectrochemical investigation of water oxidation with hematite electrodes. Energy Environ Sci 5:7626–7636

Klahr B, Gimenez S, Fabregat-Santiago F, Bisquert J, Hamann TW (2012b) Photoelectrochemical and impedance spectroscopic investigation of water oxidation with "Co-Pi"-coated hematite electrodes. J Am Chem Soc 134:16693–16700

870 Klahr B, Gimenez S, Fabregat-Santiago F, Hamann T, Bisquert J (2012c) Water oxidation at
871   hematite photoelectrodes: the role of surface states. J Am Chem Soc 134:4294–4302
872 Klahr B, Gimenez S, Zandi O, Fabregat-Santiago F, Hamann T (2015) Competitive photoelec-
873   trochemical methanol and water oxidation with hematite electrodes. ACS Appl Mater Inter-
874   faces 7:7653–7660
875 Le Formal F, Tetreault N, Cornuz M, Moehl T, Graetzel M, Sivula K (2011) Passivating surface
876   states on water splitting hematite photoanodes with alumina overlayers. Chem Sci 2:737–743
877 Li J, Peter LM (1985) Surface recombination at semiconductor electrodes. Part III. Steady-state
878   and intensity modulated photocurrents response. J Electroanal Chem 193:27–47
879 Li J, Meng F, Suri S, Ding W, Huang F, Wu N (2012) Photoelectrochemical performance
880   enhanced by a nickel oxide-hematite p-n junction photoanode. Chem Commun 48:8213–8215
881 Lin Y, Xu Y, Mayer MT, Simpson ZI, McMahon G, Zhou S, Wang D (2012) Growth of p-type
882   hematite by atomic layer deposition and its utilization for improved solar water splitting. J Am
883   Chem Soc 134:5508–5511
884 Martinson ABF, Goes MS, Fabregat-Santiago F, Bisquert J, Pellin MJ, Hupp JT (2009) Electron
885   transport in dye-sensitized solar cells based on ZnO nanotubes: evidence for highly efficient
886   charge collection and exceptionally rapid dynamics. J Phys Chem A 113:4015–4021
887 Monllor-Satoca D, Bartsch M, Fabrega C, Genc A, Reinhard S, Andreu T, Arbiol J,
888   Niederberger M, Morante JR (2015) What do you do, titanium? Insight into the role of titanium
889   oxide as a water oxidation promoter in hematite-based photoanodes. Energy Environ Sci
890   8:3242–3254
891 Peter LM (1990) Dynamic aspects of semiconductor photoelectrochemistry. Chem Rev
892   90:753–769
893 Ponomarev EA, Peter LM (1995) A comparison of intensity modulated photocurrent spectroscopy
894   and photoelectrochemical impedance spectroscopy in a study of photoelectrochemical hydro-
895   gen evolution at p-InP. J Electroanal Chem 397:45–52
896 Pyper KJ, Yourey JE, Bartlett BM (2013) Reactivity of $CuWO_4$ in photoelectrochemical water
897   oxidation is dictated by a midgap electronic state. J Phys Chem C 117:24726–24732
898 Raga SR, Barea EM, Fabregat-Santiago F (2012) Analysis of the origin of open circuit voltage in
899   dye solar cells. J Phys Chem Lett 3:1629–1634
900 Reichman J (1980) The current-voltage characteristics of semiconductor-electrolyte junction
901   photovoltaic cells. Appl Phys Lett 36:574–577
902 Riha SC, Klahr BM, Tyo EC, Seifert S, Vajda S, Pellin MJ, Hamann TW, Martinson ABF (2013)
903   Atomic layer deposition of a submonolayer catalyst for the enhanced photoelectrochemical
904   performance of water oxidation with hematite. ACS Nano 7:2396–2405
905 Rodenas P, Song T, Sudhagar P, Marzari G, Han H, Badia-Bou L, Gimenez S, Fabregat-Santiago F,
906   Mora-Sero I, Bisquert J, Paik U, Kang YS (2013) Quantum dot based heterostructures for
907   unassisted photoelectrochemical hydrogen generation. Adv Energy Mater 3:176–182
908 Salvador P, Gutierrez C (1984) The nature of surface states involved in the photo- and electrolu-
909   minescence spectra of n-titanium dioxide electrodes. J Phys Chem 88:3696–3698
910 Salvador P, Gutiérrez C (1984) Mechanisms of charge transfer at the semiconductor-electrolyte
911   interface. J Electrochem Soc 131:326–336
912 Shi X, Herraiz-Cardona I, Bertoluzzi L, Lopez-Varo P, Bisquert J, Park JH, Gimenez S (2016)
913   Understanding the synergistic effect of WO_3-$BiVO_4$ heterostructures by impedance spectros-
914   copy. Phys Chem Chem Phys
915 Steier L, Herraiz-Cardona I, Gimenez S, Fabregat-Santiago F, Bisquert J, Tilley SD, Graetzel M
916   (2014) Understanding the role of underlayers and overlayers in thin film hematite photoanodes.
917   Adv Funct Mater 24:7681–7688
918 Tench DM, Gerischer H (1977) The phototransition in ZnO at 380 nm studied by anodic
919   photocurrents. J Electrochem Soc 124:1612–1618
920 Trevisan R, Rodenas P, Gonzalez-Pedro V, Sima C, Sanchez RS, Barea EM, Mora-Sero I,
921   Fabregat-Santiago F, Gimenez S (2013) Harnessing infrared photons for photoelectrochemical
922   hydrogen generation. A PbS quantum dot based "quasi-artificial leaf". J Phys Chem Lett
923   4:141–146

Vanmaekelbergh D (1997) Direct and surface state mediated electron transfer at semiconductor/ electrolyte junctions. II. A comparison of the interfacial admittance. Electrochim Acta 42:1135–1141

Wang Q, Ito S, Grätzel M, Fabregat-Santiago F, Mora-Seró I, Bisquert J, Bessho T, Imai H (2006) Characteristics of high efficiency dye-sensitized solar cells. J Phys Chem B 110:19406–19411

Xu J, Herraiz-Cardona I, Yang X, Gimenez S, Antonietti M, Shalom M (2015) The complex role of carbon nitride as a sensitizer in photoelectrochemical cells. Adv Opt Mater 3(8):1052–1058

Yang W, Yu Y, Starr MB, Yin X, Li Z, Kvit A, Wang S, Zhao P, Wang X (2015) Ferroelectric polarization-enhanced photoelectrochemical water splitting in TiO_2–$BaTiO_3$ core–shell nanowire photoanodes. Nano Lett 15:7574–7580

Yatom N, Neufeld O, Caspary Toroker M (2015) Toward settling the debate on the role of Fe_2O_3 surface states for water splitting. J Phys Chem C 119:24789–24795

Zandi O, Hamann TW (2014) Enhanced water splitting efficiency through selective surface state removal. J Phys Chem Lett 5:1522–1526

Zhong DK, Gamelin DR (2010) Photoelectrochemical water oxidation by cobalt catalyst ("Co–Pi")/α-Fe_2O_3 composite photoanodes: oxygen evolution and resolution of a kinetic bottleneck. J Am Chem Soc 132:4202–4207